Internal Ocean Dynamics Contribution to North Atlantic Interdecadal Variability Strengthened by Ocean–Atmosphere Thermal Coupling

OLIVIER ARZEL,[a] THIERRY HUCK,[a] ANTOINE HOCHET,[a] AND ALEXANDRE MUSSA[b]

[a] *Laboratoire d'Océanographie Physique et Spatiale, Univ. Brest, CNRS, IRD, IFREMER, Brest, France*
[b] *Laboratoire Littoral, Environnement et Sociétés, La Rochelle Université, La Rochelle, France*

(Manuscript received 30 March 2022, in final form 2 September 2022)

ABSTRACT: Identifying the primary drivers of North Atlantic interdecadal climate variability is crucial for improving climatic prediction over the coming decades. Here the effect of thermal coupling on the leading energy sources of the interdecadal variability of the ocean–atmosphere system is examined by means of a stochastically forced idealized coupled model. The effect of coupling is quantified from a comparison of the buoyancy variance budget of coupled and uncoupled model configurations. The simplicity of the model allows us to contrast the effect of coupling between a supercritical regime where the deterministic ocean dynamics drive the variability and a damped regime where noise forcing is central to its existence. The results show that changes in surface buoyancy fluxes act as a sink of temperature variance in the supercritical regime, and only become a source in the strongly damped regime. By contrast, internal ocean dynamics associated with the interaction of transient buoyancy fluxes with mean buoyancy gradients always act as a source of interdecadal variability. In addition to the reduced thermal damping effect in coupled integrations, thermal coupling with the atmosphere is shown to significantly increase the role of internal ocean dynamics in the variability, particularly in the regime where interdecadal modes are damped. Only for oceanic background states in the strongly damped regime do changes in surface buoyancy fluxes play a leading role in the upper-ocean variability. A stochastically forced coupled box model is proposed that captures the basic effect of thermal coupling on atmospheric and oceanic energy sources of variability.

SIGNIFICANCE STATEMENT: The purpose of this study is to better understand the impact of ocean–atmosphere thermal coupling on the leading energy sources of Atlantic interdecadal variability. Increasing our understanding of the physical mechanisms driving climate variability at interdecadal time scales is important to improve climate prediction. We show that the effect of ocean–atmosphere thermal coupling, as measured by the atmospheric feedback on sea surface temperature anomalies, is to substantially increase the role of internal ocean dynamics in the low-frequency variability of the upper-ocean heat content and sea surface temperature. Atmospheric stochastic forcing only becomes the primary driver of the oceanic temperature variability in the large dissipative limit, when internal ocean modes are strongly damped.

KEYWORDS: Atmosphere-ocean interaction; Stochastic models; Interdecadal variability; North Atlantic Ocean; Internal variability

1. Introduction

Multidecadal variability of North Atlantic sea surface temperatures (SSTs) has been observed in both the instrumental record (Delworth et al. 2007; Deser et al. 2010; Tung and Zhou 2013) and a number of climatic proxy reconstructions (Mann et al. 1998; Gray et al. 2004; Chylek et al. 2011). Atlantic multidecadal variability (AMV; Sutton et al. 2018) is characterized by alternating basinwide decadal-scale warming and cooling periods with maximum variance at subpolar latitudes. Clement et al. (2015) suggested that the AMV could result from the thermodynamic response to atmospheric stochastic forcing and that ocean circulation variations are unimportant. This mechanism seems, however, incompatible with the paleorecord that exhibits statistically significant multidecadal periods above a red-noise background (e.g., Gray et al. 2004; Wang et al. 2017). O'Reilly et al. (2016) showed instead that ocean circulation variations are key to reproduce the sign of the observed correlation between surface heat fluxes and the AMV. Zhang et al. (2019) reviewed the observational and modeling evidence for the origins of the AMV and concluded that internal ocean dynamics is a key driver. The existence of such internal variability was recently questioned by Mann et al. (2021), who found instead a prominent role of volcanic forcing and anthropogenic aerosols. Which of internal ocean dynamics, atmospheric stochastic forcing, or external radiative forcing lies at the very origin of the observed AMV remains therefore much debated (Zhang et al. 2019). The instrumental record is unfortunately too short compared to the time scale of the variability and too sparse in terms of spatial coverage to obtain a definitive answer to this question. The present study will solely focus on the variability generated internally in the ocean–atmosphere system. Even in this context numerical models are inconclusive, in part because they show that the relative contributions of the ocean and atmosphere to the variability are a strong function of poorly constrained critical parameters, such as turbulent eddy diffusivities associated with unresolved scales (Arzel and Huck 2020). In addition, ocean–atmosphere interactions certainly have an impact on the amplitude of the variability, at least at low frequencies (Barsugli and Battisti 1998), but the net effect

Corresponding author: Olivier Arzel, oarzel@univ-brest.fr

DOI: 10.1175/JCLI-D-22-0191.1

of those interactions on the leading energy sources of the variability has yet to be found. This study will thus focus on the effect of thermal coupling, rigorously defined hereafter as the effect of the atmospheric feedback on SST anomalies, on the primary drivers of the interdecadal variability of the extratropical ocean–atmosphere system.

The effect of ocean–atmosphere coupling on the decadal or longer variability is traditionally evaluated by comparing fully coupled ocean–atmosphere simulations to "forced" ocean-only experiments where the surface heat, momentum, and freshwater fluxes are diagnosed from the coupled run. Under such flux boundary conditions atmospheric damping on SST anomalies is reduced to zero and the amplitude of oscillations is maximized. This approach has been used in many modeling studies and across a large diversity of model configurations and complexities. Delworth and Greatbatch (2000) and Gastineau et al. (2018) performed such experiments with comprehensive coupled general circulation models (GCMs) to show that coupling with the atmosphere was not essential to the variability, and that atmospheric stochastic forcing associated with midlatitudes disturbances was necessary to sustain interdecadal oscillations against dissipation. One drawback of such an approach is that the surface fluxes used to drive ocean-only integrations contain information about the response of the atmosphere to SST changes. The comparison of those ocean-only runs with coupled integrations does not therefore allow us to isolate the effect of the feedback of the atmosphere on SST anomalies, but it allows us instead to assess the entire effect of surface heat flux damping on SST anomalies. Another approach consists of forcing the ocean with the time history of surface air temperature (SAT) and winds diagnosed from an atmospheric-only integration itself forced by climatological SSTs from the coupled simulation (Barsugli and Battisti 1998). These "uncoupled" ocean-only experiments therefore lack the feedback of the atmosphere on SST anomalies. A direct comparison with the coupled runs thus allows us to unambiguously isolate the basic impact of this feedback (i.e., thermal coupling) on the variability of the coupled system. The absence of atmospheric feedback in uncoupled experiments makes the phasing of SST and SAT anomalies less coherent, leading to a smaller persistence of SST anomalies in uncoupled than in coupled integrations. The basic effect of thermal coupling is therefore to enhance the temperature variance in both the ocean and atmosphere, and more specifically at low frequencies (Barsugli and Battisti 1998). Farneti and Vallis (2011) performed uncoupled atmosphere-only experiments in the context of interdecadal climate variability and reached the same conclusions. The spectral peak at interdecadal periods in the SAT was shown to be only present when prescribed, time-varying SSTs from the coupled run were used, indicating an influence of either an oceanic interdecadal mode or some form of coupled interaction. Wu and Liu (2005) ran an uncoupled experiment with their realistic coupled model to show the critical role of coupling in sustaining North Atlantic Ocean decadal variability. Garuba et al. (2018) showed on the basis of coupled and partially coupled integrations of a realistic coupled climate model that the AMV is mostly driven by ocean circulation variability.

Arzel and Huck (2020) used a realistic ocean general circulation model forced by combination of steady surface buoyancy and momentum fluxes and North Atlantic Oscillation (NAO)-related stochastic forcing to show that internal ocean dynamics plays a leading role in the growth of SST variance in the supercritical regime (i.e., the regime where the multidecadal variability develops without any noise forcing, at relatively low diffusivities), but that the atmospheric stochastic forcing represents the major energy source for the variability in the damped regime (i.e., the regime where the variability requires some atmospheric noise to emerge, at relatively high diffusivities). Therefore, the leading energy source of the variability is a strong function of critical parameters (such as eddy diffusivities) and background climate conditions, at least in the forced case. How ocean–atmosphere thermal coupling modifies this behavior remains to be determined. The present study will assess the impact of thermal coupling on the leading energy sources of the variability and is therefore a natural extension of Arzel and Huck (2020), who used an ocean-only configuration. The aim of the present study is thus to progress in the understanding of the physical processes driving Atlantic climate variability at interdecadal time scales. The main purpose is to quantify the impact of ocean–atmosphere thermal coupling on the *drivers* of temperature variance at interdecadal time scales. As such the present study is also a natural extension of Barsugli and Battisti (1998), who focused their analysis on the impact of coupling on the temperature variance of the ocean–atmosphere system. A joint objective is to determine how thermal coupling impacts the energy sources of the variability in both the supercritical and damped regimes. Different variability regimes will be obtained by systematically varying the magnitude of the turbulent eddy diffusivity K, which has been shown to be one of the most critical parameters to the interdecadal variability of the overturning circulation (Huck et al. 1999a). For each value of K, the effect of the atmospheric feedback on SST anomalies is inferred from a comparison of coupled and uncoupled integrations. These simulations are supplemented by forced integrations to assess the impact of surface heat flux damping associated with coupling. Given the relatively large number of millennial-scale experiments required to achieve this task, a computationally efficient coupled model is required. Following the views of Held (2005) we believe that the use of a model hierarchy such as the one proposed here is necessary to help gain understanding of the mechanisms driving climate variability at interdecadal time scales. The model comprises a planetary geostrophic oceanic component coupled to a stochastically forced energy balance model. The geometry is idealized with a two-hemisphere sector of sphere and a southern periodic channel. The model captures the large-scale features of the Atlantic circulation and for some parameter range exhibits interdecadal oscillations under deterministic forcing conditions. The cause of the variability was shown to be a large-scale baroclinic instability of the mean flow driving interdecadal oscillations with the oscillation period set by the zonal transit time of long baroclinic planetary waves (Colin de Verdière and Huck 1999; te Raa and Dijkstra 2002). This mode of variability has been shown to persist in realistic configurations of ocean-only (Sévellec and Fedorov 2013; Arzel

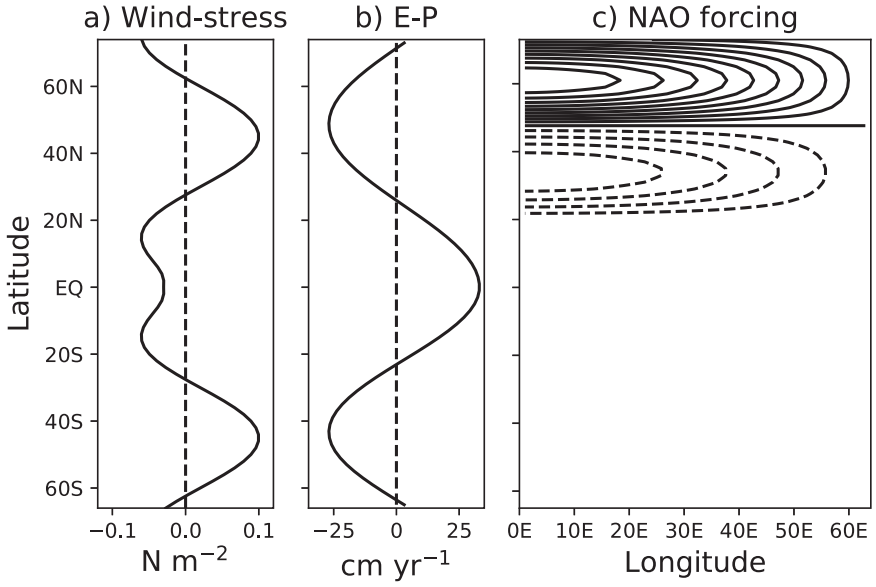

FIG. 1. (a) Zonal (solid) and meridional (dashed) surface wind stress. (b) Imposed freshwater forcing (evaporation minus precipitation), (c) spatial pattern of the stochastic forcing (contour interval = 10 W m^{-2}) entering the atmospheric thermodynamic balance. The amplitude in the subpolar gyre (100 W m^{-2}) is twice that of the subtropical gyre (50 W m^{-2}) similar to Herbaut et al. (2002). The sign change in the stochastic forcing roughly occurs at the intergyre boundary at 47°N.

et al. 2018) and coupled models (Ortega et al. 2015; Muir and Fedorov 2017; Gastineau et al. 2018).

The outline of this paper is as follows. Section 2 provides a description of the idealized coupled ocean–atmosphere model as well as the experimental procedure used to quantify the effect of ocean–atmosphere thermal coupling. The main characteristics of the variability are presented in section 3, and its sensitivity to horizontal turbulent diffusivity is presented in section 4 for the coupled, uncoupled, and forced cases. Section 5 quantifies the leading energy sources of the interdecadal variability and their sensitivity to K using an approach based on the buoyancy variance budget. The model hierarchy is finally extended to a coupled stochastically forced ocean–atmosphere dynamical system in section 6 that reproduces with very high fidelity the results obtained with the 3D model. The results are then summarized and discussed in section 7.

2. Model and experiments

a. The coupled model

The dynamics of the 3D ocean model is governed by the planetary geostrophic equations, appropriate for horizontal scales of motion much larger than the deformation radius (Salmon 1986; Colin de Verdière 1988). The model is spherical with a 2° horizontal resolution, and extends from 66°S to 74°N and is 64° wide in longitude. The ocean has a constant depth (4500 m) divided into 15 levels with vertical grid spacing increasing from 50 m near the surface to 550 m near the bottom. A periodic channel is introduced in the south of the domain (66°–52°S) to represent an Antarctic Circumpolar Current (ACC)-like flow. No-slip and no-flux boundary conditions are applied at solid boundaries. Static instability is removed by instantaneously restoring vertical density profiles to neutrality. A linear equation of state is used with constant thermal expansion and haline contraction coefficients. The vertical mixing for tracers is constant and fixed to 10^{-4} m^2 s^{-1}, consistent with observational estimates of the abyssal stratification and global upwelling (Munk and Wunsch 1998). The horizontal Laplacian friction is also constant and fixed to 10^5 m^2 s^{-1}. The surface wind stress forcing is distributed over the surface layer (50 m depth); it is purely zonal and follows the analytical profile function of latitude proposed by Weaver and Sarachik (1990) (Fig. 1a).

The oceanic model is coupled to a dry energy balance atmospheric model similar to that developed by Fanning and Weaver (1996). The freshwater forcing is imposed and follows the latitudinal profile shown in Fig. 1b. The atmospheric eddy temperature diffusivity K_a is uniform and fixed to 1.3×10^6 m^2 s^{-1}. The atmosphere–ocean heat exchange coefficient λ falls within the range of observed values and is fixed to 30 W m^{-2} K^{-1} in all experiments. Both the incoming solar radiation S at the top of the atmosphere and the planetary albedo α_p follow annual mean latitudinal profiles given by North et al. (1981) and Graves et al. (1993), respectively. In the absence of atmospheric dynamics, stochastic forcing is introduced in the atmospheric temperature equation as

$$Q_N(x, y, t) = \sigma_N Q_{\mathrm{NAO}}(x, y)\zeta(t), \tag{1}$$

This term parameterizes the stochastic forcing associated with the divergence of eddy temperature fluxes, which are typically

enhanced at midlatitudes. There the observed transient sensible and latent heat fluxes amount to about $P = 3.5$ PW (Peixoto and Oort 1992). Using an eddy length scale L_{eddy} of 1000 km and a zonal length scale L_x of 25 000 km for the length of a latitude circle at midlatitudes, we obtain $\sigma_N = P/L_x L_{\text{eddy}} = \mathcal{O}(100)\,\text{W m}^{-2}$ for the amplitude of the eddy forcing. We then specify $\sigma_N = 100\ \text{W m}^{-2}$ in all stochastically forced experiments. The pattern Q_{NAO} is similar to that used by Herbaut et al. (2002). It mimics the observed North Atlantic Oscillation pattern with a dipolar structure centered at midlatitudes and with maximum values in the west of the basin. The stochastic time series $\zeta(t)$ obeys a first-order autoregressive process with an e-folding time scale of 10 days, a value consistent with observational estimates (Feldstein 2000). To assess the effect of noise coherence additional experiments using a white noise forcing and a longer temporal coherence (30 days) have been conducted. The noise forcing has a sampling frequency (0.05 days) corresponding to the oceanic time step of the model. The variance of $\zeta(t)$ is 1. Note finally that the stochastic time series are strictly identical in all stochastically forced integrations.

b. Experimental design

Three different model configurations (coupled, uncoupled, forced) are used to assess the impact of coupling on the variability. For each of those three configurations the model is run with and without atmospheric stochastic forcing. The latter case is said to be deterministic. This procedure is repeated for a wide range of oceanic horizontal eddy diffusivities K between 500 and 2600 $\text{m}^2\,\text{s}^{-1}$. Those values approximately cover the observed range in the North Atlantic (Abernathey and Marshall 2013), but the observed large spatial variations of these coefficients are not captured. This approach allows us to explore the effect of coupling in two different variability regimes, namely a supercritical regime where the variability spontaneously develops without atmospheric stochastic forcing and a damped regime where the variability requires some noise to emerge. Deterministic runs are integrated for 5000 years and are initialized from a resting ocean with uniform temperature (4°C) and salinity (35 psu). Stochastic runs are integrated for 1000 years and are initialized from the end state of deterministic runs.

1) COUPLED

The model is integrated in its standard coupled mode (denoted by superscript C) where the atmospheric temperature T_a and the surface buoyancy (heat and freshwater) flux B_O toward the ocean are given by

$$C_a dT_a^C/dt = F(T_a^C, T_o^C) + Q_N, \tag{2}$$

$$B_O^C = G(T_a^C, T_o^C), \tag{3}$$

where C_a is the atmospheric heat capacity and T_o the sea surface temperature. The operators F and G include both turbulent and radiative fluxes,

$$F(T_a, T_o) = \lambda(T_o - T_a) + \epsilon_o \sigma T_o^4 - \epsilon_a \sigma T_a^4 - \epsilon_p \sigma T_a^4 + S a_s (1 - \alpha_p) + K_a \nabla^2 T_a, \tag{4}$$

$$B_O(T_a, T_o) = \lambda(T_a - T_o) - \epsilon_o \sigma T_o^4 + \epsilon_a \sigma T_a^4 + S(1 - a_s)(1 - \alpha_p), \tag{5}$$

where σ is the Stefan-Boltzmann constant, $\epsilon_o = 0.96$ is the longwave emissivity of the surface, $\epsilon_a = 0.85$ is the longwave emissivity of the atmosphere, $\epsilon_p = 0.63$ is the planetary emissivity to space, and $a_s = 0.3$ is the shortwave absorptivity. The terms on the right-hand side of (4) are, from first to last, the sensible heat exchange with the surface, the upward longwave emission from the surface, the downward longwave emission from the atmosphere, the outgoing longwave radiation to space, the absorbed solar radiation within the atmosphere, and the diffusive heat transport. The last term on the right-hand side of (5) is the absorbed solar flux at the surface.

2) UNCOUPLED

In phase 1 the atmosphere is first run with the fixed 100 years averaged SST distribution diagnosed from deterministic coupled integrations. This SST field is defined here as the climatological SST field T_o^{clim}. In phase 2 the ocean model is then forced by the surface fluxes computed using the time history of atmospheric temperatures from the first phase and the actual SST field from the uncoupled integration. Those two phases are run synchronously with the same coupling frequency as the coupled model (0.05 days). Hence

$$C_a dT_a^U/dt = F(T_a^U, T_o^{\text{clim}}) + Q_N, \tag{6}$$

$$B_O^U = G(T_a^U, T_o^U), \tag{7}$$

where the superscript U stands for uncoupled. In those uncoupled runs the atmospheric temperature can only change in response to the stochastic forcing, with all other forcings including the SST field being kept constant in time. The atmosphere therefore does not see the SST variations that can occur in response to either atmospheric stochastic forcing (if any, embedded in T_a^U) or changes due to the existence of an intrinsic interdecadal ocean mode. In the coupled integrations by contrast the atmosphere can vary in response to both atmospheric stochastic forcing and changing SSTs. The comparison of the coupled and uncoupled runs therefore allows us to unambiguously isolate the impact of the atmospheric feedback on SST anomalies.

3) FORCED

The procedure here is very similar to that used for building uncoupled runs except for the second phase, where the surface heat flux to the ocean B_O^F is now computed using the climatological SST T_o^{clim} rather than the actual SST obtained in those ocean-only integrations,

$$B_O^F = G(T_a^U, T_o^{\text{clim}}), \tag{8}$$

where the superscript F stands for forced.

At this stage, it is crucial to emphasize the central difference that exists between the "forced" and "uncoupled" runs

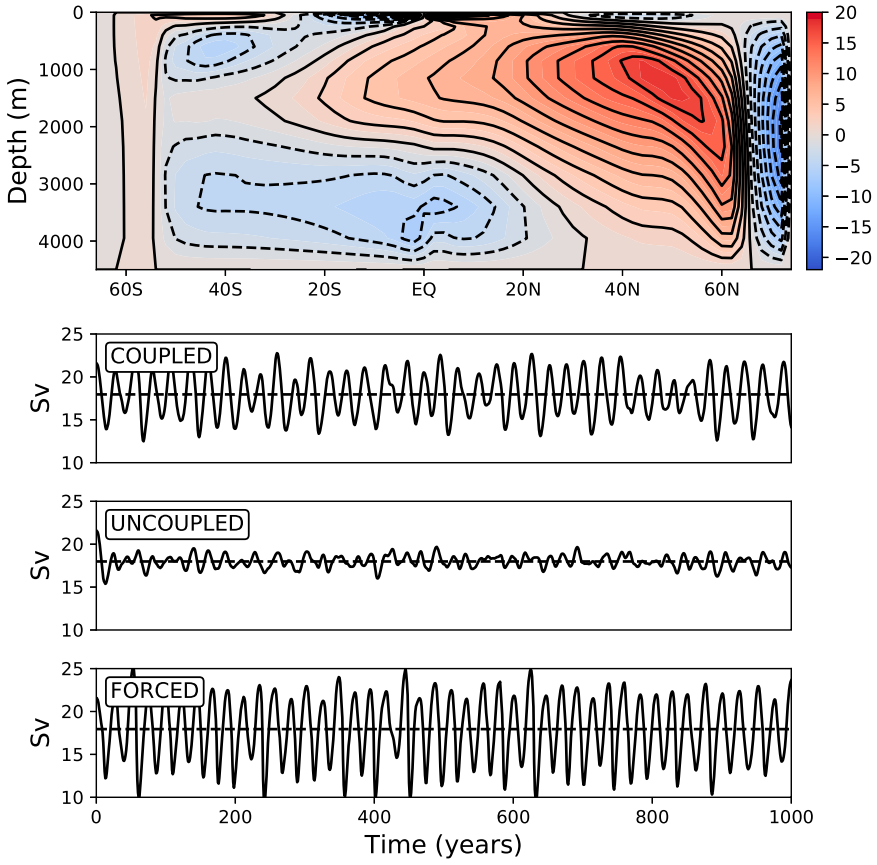

FIG. 2. (top) Time-mean meridional overturning circulation (MOC) in the stochastic coupled integration for $K = 1000\ \mathrm{m^2\ s^{-1}}$. (bottom) Time series of the MOC index in the stochastic experiments. The MOC index is defined as the maximum of the meridional overturning streamfunction north of 30°N and below 850 m. The stochastic experiments are run for 1000 years and start from the end state of the corresponding deterministic solutions. These later solutions are obtained from a 5000-yr-long integration which was necessary to reach statistical equilibrium.

that will be used in this study. Forced runs are ocean-only integrations driven by imposed surface buoyancy fluxes. The surface heat flux damping on SST anomalies, referred to as *thermal damping* hereafter, is therefore reduced to zero in those experiments. As a result, the amplitude of the variability in the forced runs is maximized. By contrast uncoupled runs have increased surface heat flux damping on SST anomalies since the absence of atmospheric feedback on SST anomalies in those experiments makes the phasing between SST and SAT anomalies less coherent. Uncoupled runs have, therefore, a much weaker variability than either the forced or coupled runs. The comparison of coupled and forced integrations allows us to assess the effect of the entire surface heat flux damping associated with air–sea coupling on the variability. This is a traditional approach that helps determine whether the variability obtained in the coupled model can be interpreted as an excitation of a damped ocean mode (Delworth and Greatbatch 2000) or as a manifestation of a self-sustained ocean mode where noise forcing is not essential (Gastineau et al. 2018). The comparison of uncoupled and coupled runs, by contrast, allows us to determine the effect of the atmospheric feedback on SST anomalies on the variability. Coupling with the atmosphere is obviously absent in the forced experiments but the effect of the atmospheric feedback on SST anomalies, referred to as thermal coupling in the present study, can only be determined from the comparison of coupled and uncoupled runs.

3. Interdecadal variability

In what follows we focus on the stochastic integrations and contrast the variability patterns obtained for the coupled, uncoupled, and forced systems. The comparison is made for the canonical horizontal eddy diffusivity value $K = 1000\ \mathrm{m^2\ s^{-1}}$.

Figure 2 shows the time-mean meridional overturning streamfunction in the stochastic coupled run, as well as the time series of the MOC index over a 1000-yr period for the coupled, uncoupled, and forced systems. The MOC index is defined as the maximum value of the meridional overturning streamfunction north of 30°N and below 850 m. Despite the relative simplicity of the model, in terms of both geometry and physics, the observed North Atlantic meridional overturning circulation is well

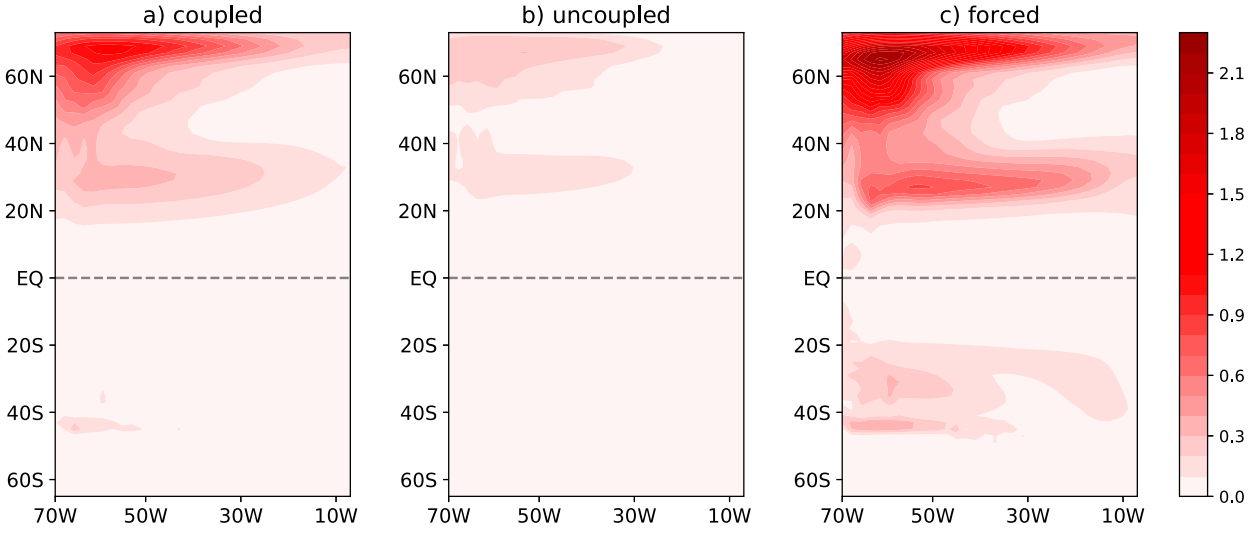

FIG. 3. SST standard deviations diagnosed from the annual mean output of SST anomalies over a 100-yr period for the stochastic case with $K = 1000\ \mathrm{m^2\ s^{-1}}$ for the (a) coupled, (b) uncoupled, and (c) forced configurations.

reproduced with a thermally direct cell intensified in the Northern Hemisphere with a peak value close to that observed (18 Sv, where $1\ \mathrm{Sv} \equiv 10^6\ \mathrm{m^3\ s^{-1}}$; Colin de Verdière et al. 2019), and a weaker (5 Sv) thermally indirect cell at depth reminiscent of the Antarctic Bottom Cell. Quasi-regular oscillations with interdecadal periods (~25 years) are found in all cases, with peak-to-peak amplitudes reaching 38% (56%) of the mean transport in the coupled (forced) case, but only 12% in the uncoupled system. Thermal coupling with the atmosphere, as inferred from the comparison between the coupled and uncoupled systems, therefore acts as a strong amplifier of interdecadal oscillations in agreement with Farneti and Vallis (2011) and Wu and Liu (2005). As originally stated by Barsugli and Battisti (1998), coupling with the atmosphere causes SST and SAT anomalies to vary more in phase in the coupled case, thereby reducing the damping on SST anomalies compared to the uncoupled case. In the forced case the damping of SST anomalies is at its minimum (but nonzero because of the presence of mixing processes), leading to much greater variability. This feature can be seen in the standard deviations of SST anomalies in Fig. 3. For all cases SST variance is maximum in the northwest corner of the basin and is about 3 times greater in the coupled compared to the uncoupled case. There is virtually no variability in the Southern Hemisphere: the weakening of the upper-ocean circulation in the Southern Hemisphere caused by the periodic channel makes the flow more stable with respect to the large-scale instability mechanism and no variability emerge (Arzel et al. 2007). The spectral peaks (Fig. 4) in both the MOC index and SST anomalies (computed as the weighted average in the region of maximum SST variance, i.e., 46°–74°N, 70°–50°E) greatly exceed the red-noise background (but barely for the uncoupled case, which just passes the 95% confidence level), indicating that interdecadal oscillations cannot be simply interpreted as an integration of the atmospheric noise by the oceanic mixed layer. The first and second leading patterns of variability have been estimated in terms of empirical orthogonal functions (EOFs) and are presented in Fig. 5. The patterns in the coupled and forced systems are very similar but with a greater amplitude for the latter. The first EOF features a monopole intensified in the northwestern corner of the basin, whereas the second EOF features a monopole of opposite sign centered in the subtropics and with a much weaker amplitude. These two EOFS vary in quadrature (not shown) with the first EOF leading the second one by about 6 years, thereby covering a full cycle in about 25 years. A lagged regression analysis between SST anomalies and the MOC index highlights the emergence and growth of perturbations in the eastward extension of the western boundary current in the northwestern corner of the basin (not shown). The perturbations then propagate westward toward the western boundary where they subduct and quickly dissipate (not shown). This spatiotemporal organization of the variability is similar to several previous idealized ocean-only model studies using fixed flux boundary conditions without noise forcing (Greatbatch and Zhang 1995; Colin de Verdière and Huck 1999; te Raa and Dijkstra 2002). In the uncoupled case, the NAO signature along with its dipolar structure is clearly evident in the first EOF of SST anomalies (Fig. 5). Therefore, the atmospheric feedback on SST anomalies not only increases the amplitude of the mode but also significantly alters the leading pattern of the variability, at least for this specific value of $K = 1000\ \mathrm{m^2\ s^{-1}}$. The second EOF of the uncoupled case exhibits strong similarities with the leading EOF of the coupled and forced cases, suggesting an implication of internal ocean dynamics in the uncoupled variability.

4. Sensitivity to K

Figure 6 presents the sensitivity of some key quantities to the horizontal diffusivity K in the coupled, uncoupled, and forced systems, and under both deterministic and stochastic forcing conditions. We first see that the strength of the mean

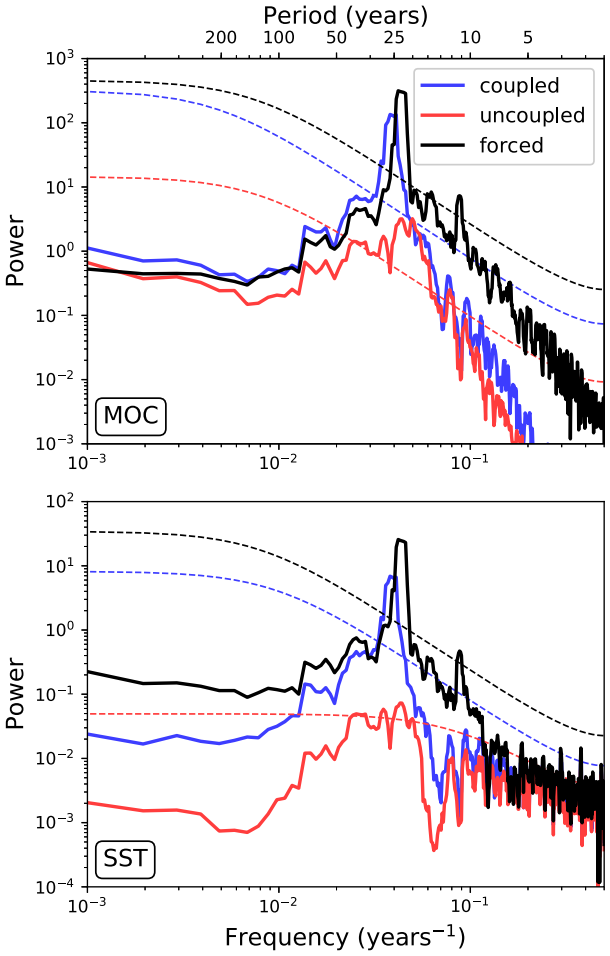

FIG. 4. Power spectra of (top) the MOC index (Sv^2 years) and (bottom) SST anomalies (°C^2 years) time series averaged in the northwest corner (70°–50°W and north of 46°N) in the stochastic experiments with $K = 1000$ m^2 s^{-1} and for the coupled (blue), uncoupled (red), and forced (black) systems. The calculation uses a multitaper technique with three tapers and is based on 1000 years of annual mean model output. The smooth dashed lines indicate the red noise 95% confidence level.

overturning increases with K in all cases. This behavior sharply contrasts with results obtained with models where the eddy-induced diffusivity rather than the horizontal diffusivity is varied (Marshall et al. 2017; Arzel and Huck 2020). The reason for this discrepancy may be caused by the "Veronis effect" whereby horizontal diffusion induces large diapycnal fluxes once the isopycnals are tilted by coastal upwellings, in particular along the western boundary (Veronis 1975; Huck et al. 1999b). Quite remarkably the strength of the mean overturning for a given value of K keeps nearly the same value whatever configuration is used (coupled, forced, uncoupled) and irrespective of the stochastic forcing being present or not. Hence rectification of the mean flow by stochastic forcing does not occur in our simulations, as opposed to in those of Frankcombe and Dijkstra (2009). This implies that the different variability characteristics associated with the coupled, uncoupled, and forced systems, in particular when stochastic forcing is present, cannot be ascribed to modifications of the mean circulation.

The transition from a steady circulation to an interdecadal oscillatory behavior was shown to occur through a Hopf bifurcation as the horizontal diffusivity (Colin de Verdière and Huck 1999) or ocean–atmosphere heat exchange coefficient (Chen and Ghil 1996) is decreased. Here Hopf bifurcations under deterministic conditions are successively found at $K = 210$, 1140, and 1560 m^2 s^{-1} for the uncoupled, coupled, and forced cases respectively (note that only the last two bifurcations are shown in Fig. 6). This sequence of bifurcations is consistent with the magnitude of atmospheric damping acting on SST anomalies, which is at its largest in the uncoupled case and at its lowest in the forced case, as discussed in section 2b. The suppression of variability for large K is not caused by changes in the circulation, which favors increasingly baroclinically unstable situations as K increases (Fig. 6a), but instead by the direct damping effect of dissipation on perturbations. When stochastic forcing is present interdecadal variability exists over the full range of diffusivities explored here, but only as long as the noise forcing has some temporal coherence, in agreement with Frankcombe and Dijkstra (2009) and Arzel and Huck (2020). Additional spectral analyses of the MOC and SST (averaged in the region 46°–74°N, 70°–50°W) indices show that the interdecadal variability is always statistically significant in both fields, even for the most diffusive cases. The effect of stochastic forcing on the variability is large in the damped regime (for diffusivity values larger than the critical value at bifurcation) and much weaker in the supercritical regime (for diffusivity values weaker than the critical value at bifurcation). The comparison of coupled and uncoupled configurations of the model clearly shows that thermal coupling between the ocean and atmosphere increases the temperature variance in both fluids, in agreement with Barsugli and Battisti (1998), as well as the amplitude of ocean circulation changes. The novel aspect is that the amplifying effect of thermal coupling on the variability is much stronger in the supercritical than in the damped regime. For SST for instance, thermal coupling typically quadruples the amplitude of the variability in the supercritical regime (from 0.55° to 2.31°C for $K = 500$ m^2 s^{-1}) but less than doubles it in the damped regime (from 0.28° to 0.45°C for $K = 2600$ m^2 s^{-1}). Let us finally mention that the amplitude of the changes in surface heat flux (diagnosed from a composite analysis identical to that used for SST and SAT in Fig. 6) in the region of maximum SST variance are relatively independent of K and amount to about 25 W m^{-2} (not shown), an amplitude comparable to the observed annual mean changes in turbulent fluxes associated with the NAO (e.g., Fig. 1 in Arzel and Huck 2020).

5. Energy sources

We now turn to the analysis of the effect of thermal coupling on the leading energy sources of the variability. These energy sources are identified as the major terms driving the growth of buoyancy variance in the ocean against all sources of damping. As such the buoyancy variance budget provides a quantitative estimate of the contribution of the ocean and

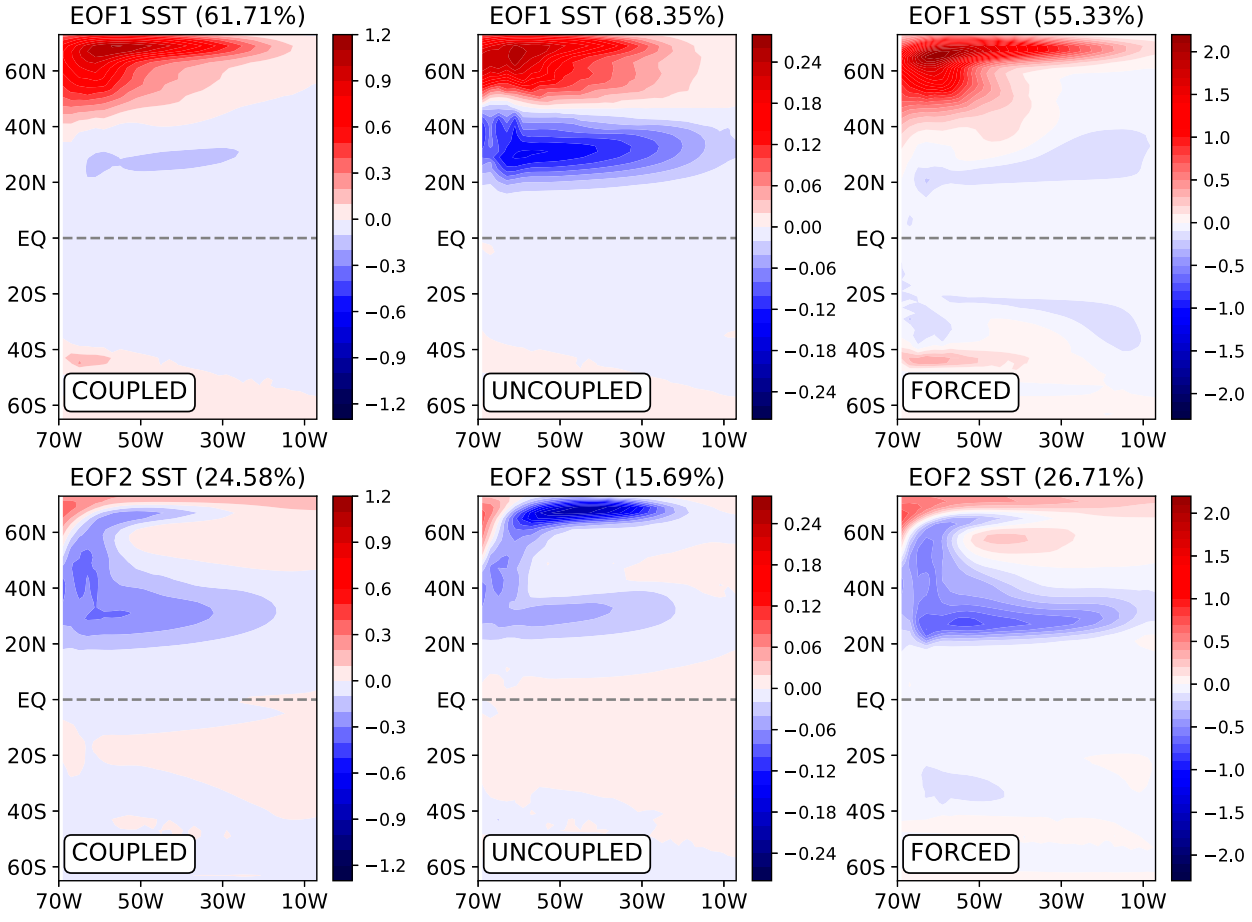

FIG. 5. (top) First and (bottom) second EOFs of annual mean SST anomalies along with the explained variance (%) in the stochastic experiments with $K = 1000\ \mathrm{m^2\ s^{-1}}$ and for the (left) coupled, (center) uncoupled, and (right) forced cases.

atmosphere to the growth of perturbations. This powerful tool has been previously and successfully used to decipher the physics of interdecadal climate variability, as simulated by both idealized and realistic ocean-only (Colin de Verdière and Huck 1999; Arzel et al. 2006, 2018) and coupled models (Arzel et al. 2007, 2012; Buckley et al. 2012; Jamet et al. 2016; Gastineau et al. 2018).

a. Method

The linearized buoyancy variance equation is given by

$$\frac{1}{2}\frac{\overline{\partial b'^2}}{\partial t} = -\overline{\mathbf{u}_h' b'} \cdot \boldsymbol{\nabla}_h \overline{b} - \overline{w' b'}\,\partial_z \overline{b} - \frac{1}{2}\overline{\mathbf{u}} \cdot \boldsymbol{\nabla}\overline{b'^2} + \overline{b' Q_b'} + \overline{b' D_b'}, \tag{9}$$

where the overbar denotes the time mean and the prime the anomaly. Integrated over the domain and weighted appropriately, it provides an equation for the available potential energy in the quasigeostrophic approximation (Huang 1998). Advection of buoyancy variance by the anomalous flow is between one and three orders of magnitude smaller than $-\overline{\mathbf{u}' b'} \cdot \boldsymbol{\nabla}\overline{b}$ for all values of K (not shown) and has consequently been removed during the linearization process. The first term on the right-hand side $-\overline{\mathbf{u}_h' b'} \cdot \boldsymbol{\nabla}_h \overline{b}$, with $\mathbf{u}_h$ being the horizontal Eulerian velocity, has been shown to dominate the growth of buoyancy variance in several ocean-only and coupled climate models (see references above). This term is central to the baroclinic instability mechanism where perturbations draw energy from the potential energy of the mean flow. Under such unstable conditions, kinetic energy of the perturbations increases through the positive exchange term $\overline{w' b'}$ and the second term in (9) therefore becomes a sink of buoyancy variance (given $\partial_z \overline{b} > 0$ in stably stratified waters). Buoyancy variance is spatially redistributed across the basin by the three-dimensional mean flow $\overline{\mathbf{u}}$ through the third term. This term is less fundamental than the first one because its global integral is zero. However, this term can either increase or decrease the variance locally and becomes comparable to the first term. The fourth term represents the growth of buoyancy variance due to the correlation between the surface buoyancy anomalies and the surface buoyancy flux anomalies $Q_b' = g_0 a_T Q'/C_O$ (with g_0 being the acceleration of gravity at the sea surface, C_O the specific heat capacity of the forcing layer, and Q' the anomalous surface heat flux). The dissipation term $\overline{b' D_b'}$ sums up contributions from horizontal and vertical mixing processes (including convective mixing) and is

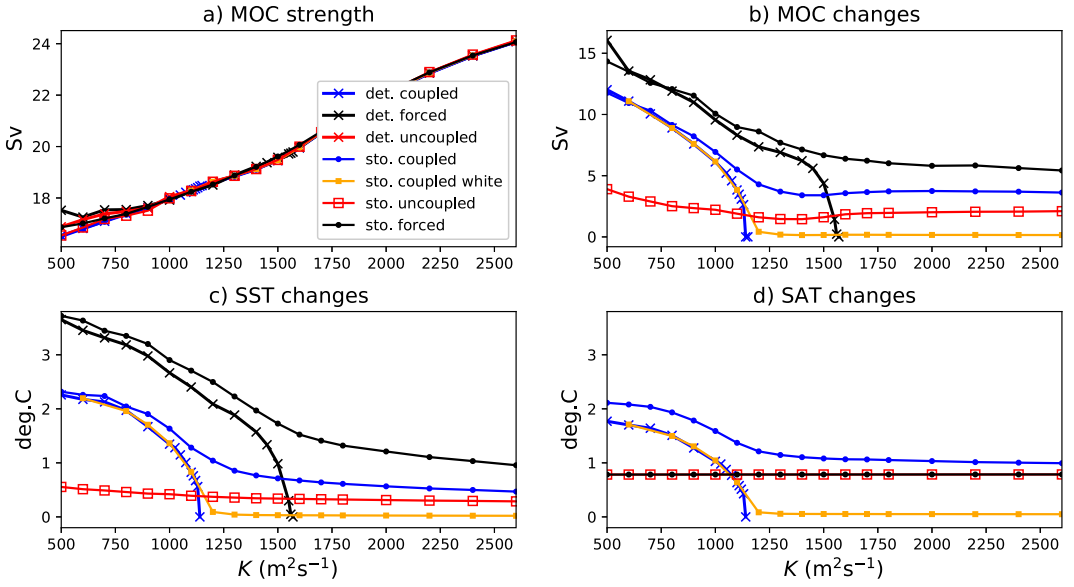

FIG. 6. Statistics of key indices as a function of the horizontal eddy diffusivity K under deterministic and stochastic forcing conditions for the coupled, uncoupled, and forced cases. (a) Time-mean MOC index. The index is defined as the maximum value of the meridional overturning streamfunction north of 30°N and below 850 m. (b) Amplitude of MOC variations (Sv). (c) Amplitude of SST changes (°C) averaged in the northwestern corner (46°–74°N, 70°–50°W), which corresponds to the region of largest temperature changes in all experiments. (d) As in (c), but for the SAT (°C). The amplitude of the variability in (b)–(d) has been estimated from a composite analysis of the last 1000 years of each experiment where the max (min) of the time series is computed as the time average of the values greater (smaller) than the mean plus (minus) one standard deviation. Note that only the changes greater than zero are shown. The uncoupled deterministic system does not have variability in the range of diffusivity values shown here. When the stochastic forcing is white (orange dotted line) the amplitude of the variability in the damped regime is greatly reduced compared to a situation where a noise forcing has a finite temporal coherence.

always a sink of buoyancy variance. In what follows, we will restrict our attention to the only two terms in (9) that can take positive values at the basin scale, namely the atmospheric energy source associated with surface buoyancy fluxes anomalies and the oceanic energy source associated with the interaction of transient buoyancy fluxes with mean horizontal buoyancy gradients.

b. Results

The buoyancy variance budget is applied to the northwestern corner of the basin (46°–74°N, 70°–50°W), which roughly coincides with the region of maximum buoyancy changes in all experiments (Fig. 3). The buoyancy changes are largely controlled by temperature variations so that the buoyancy variance budget presented hereafter is to a large extent identical to the temperature variance budget (not shown). We define the quantities $S_A = \langle \overline{b' Q_b'} \rangle$ and $S_O = -\langle \overline{\mathbf{u}_h' b'} \cdot \boldsymbol{\nabla}_h \overline{b} \rangle$, where the angle brackets denote volume averaging. The analysis entirely focuses on the budget within the uppermost 250 m of the ocean model. Because our region of averaging encompasses the bulk of the variability the advection of buoyancy variance into or out of the region by the mean flow is always an order of magnitude smaller than S_O (not shown).

Figures 7a and 7b present the sensitivity of S_O and S_A to K for the coupled, uncoupled, and forced systems, and under both deterministic and stochastic forcing conditions. We first see that S_O is positive for all model configurations and for all values of K. Consistent with the amplitude of the variability, the largest values of S_O are obtained for the forced system, and the lowest values for the uncoupled one. The oceanic energy source term in the coupled case is about an order of magnitude larger than that in the uncoupled one. The effect of the atmospheric feedback on SST anomalies is therefore to significantly increase the creation of buoyancy variance by internal ocean dynamics for all values of K, with the strongest impact in the supercritical regime (Fig. 7c).

Focusing now on S_A in the coupled case, we see that this term is strongly negative in the supercritical regime and even beyond (up to $K = 1400$ m^2 s^{-1}; Fig. 7b). In this range of K values, surface heat flux anomalies therefore act to damp the variability. For larger K values, S_A becomes positive, which along with S_O contributes to the production of buoyancy variance in the northwestern corner of the domain. The change in the sign of S_A with K can be rationalized as follows. Density anomalies are largely controlled by temperature changes so that $b' \propto T'$. Using this result, and assuming that the upwelling and downwelling longwave radiative fluxes nearly cancel out, the covariance term between the surface buoyancy flux anomalies and the buoyancy anomalies can be approximated as $S_A \propto \langle \lambda(\overline{T' T_a'} - \overline{T'^2}) \rangle$, where λ is the air–sea heat exchange coefficient (recall that both the solar and freshwater forcings are steady). Now in the supercritical regime, SST anomalies

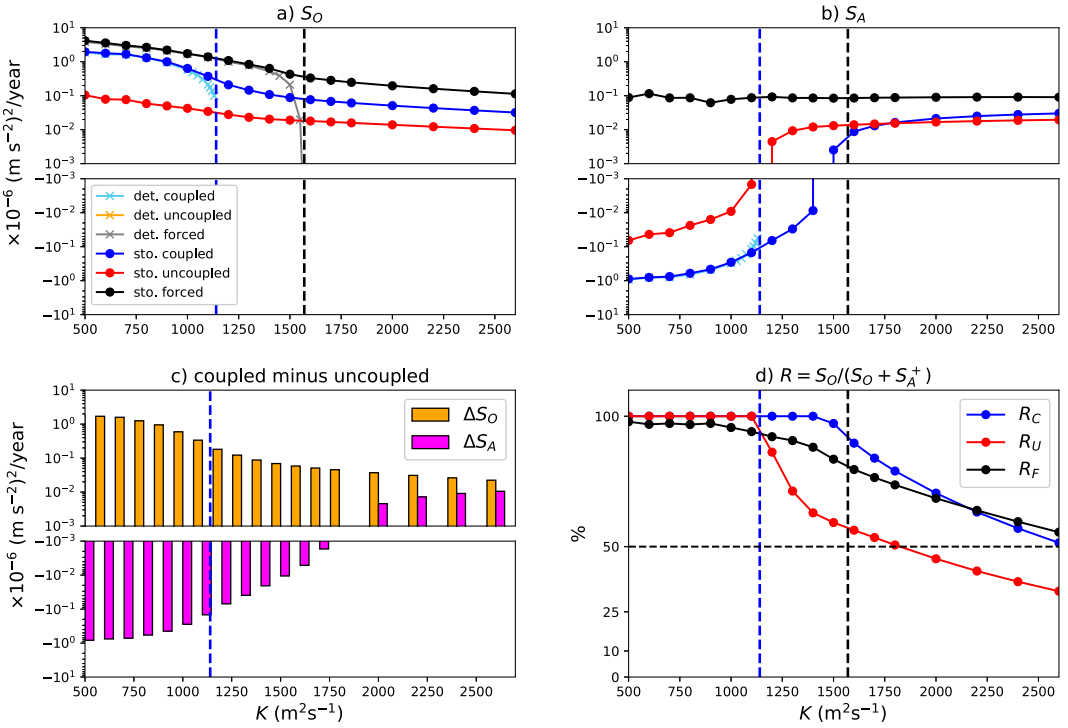

FIG. 7. Buoyancy variance budget in the northwestern corner of the domain (46°–74°N, 70°–50°W) and in the uppermost 250 m as a function of the horizontal diffusivity K. (top left) Oceanic $S_O = -\langle \overline{\mathbf{u}_h' b'} \cdot \boldsymbol{\nabla}_h \bar{b} \rangle$ and (top right) atmospheric $S_A = \langle \overline{b' Q_b'} \rangle$ energy source terms under both deterministic and stochastic boundary conditions and for the coupled, uncoupled, and forced systems. The uncoupled case under deterministic forcing conditions does not exhibit variability in the range of diffusivities considered here, which explains why it is absent. (bottom left) The changes (coupled minus uncoupled) in atmospheric and oceanic source terms caused by coupling with the atmosphere. Note that a log vertical scale is used for both positive and negative values in the top- and bottom-left panels. (bottom right) The contribution $R = S_O/(S_O + S_A^+)$ (%) of internal ocean dynamics to the production of buoyancy variance in the northwestern corner of the domain for the coupled (R_C), uncoupled (R_U), and forced (R_F) cases, with $S_A^+ = S_A$ if $S_A > 0$ and 0 otherwise (see text for details). In all panels the vertical dashed lines indicate the position of the Hopf bifurcation of the coupled (blue; $K = 1140$ m^2 s^{-1}) and forced (black; $K = 1560$ m^2 s^{-1}) cases.

are relatively large, implying that the covariance term S_A is dominated by $-\lambda\langle \overline{T'^2} \rangle$, which is always negative. Larger negative values of S_A are obtained in the coupled case in the supercritical regime because of the much greater oceanic temperature variance $\overline{T'^2}$ compared to the uncoupled case. In the damped regime, SST anomalies have a much weaker magnitude and the leading term in S_A is $\lambda\langle \overline{T' T_a'} \rangle$, which is positive since both SST and SAT anomalies tend to vary in phase. In the uncoupled system, the same behavior occurs but the change in S_A occurs for lower values of K, consistent with the lower SST variance compared to the coupled case.

Interestingly the change in the sign of S_A in the uncoupled case occurs near the Hopf bifurcation of the coupled system. Whether this occurs by pure coincidence or not remains to be found. Consistent with the larger SST variance in the coupled system compared to the uncoupled one, thermal coupling acts to increase the sink of buoyancy variance associated with surface fluxes across a large range of K values, up to 1700 m^2 s^{-1} beyond the bifurcation at 1140 m^2 s^{-1}, but to increase the production of buoyancy variance for the most diffusive cases (Fig. 7c).

In the forced case surface flux anomalies are always a source of buoyancy variance (Fig. 7). We also note that S_A in this case is nearly independent of K despite the significant changes in the amplitude of the variability between the supercritical and damped regimes. An explanation for this behavior was provided by Arzel and Huck (2020). First, the kinetic energy variability is much weaker in the damped than in the supercritical regime. Second, numerical experiments with a planetary geostrophic component similar to the present one reveal that temperature anomalies are mostly constrained by anomalous advection rather than mean flow effects (Huck et al. 1999a). Weak anomalous oceanic advection in the damped regime prevents the noise-forced SST anomalies to escape quickly from the forcing region, thereby increasing the correlation between the surface heat fluxes and the SST anomalies. The larger correlation in the damped regime compensates for the smaller SST variance resulting in a nearly constant covariance term S_A as K varies. Compared to the forced system, the coupled system decreases the production of buoyancy variance associated with both the surface fluxes and internal ocean dynamics.

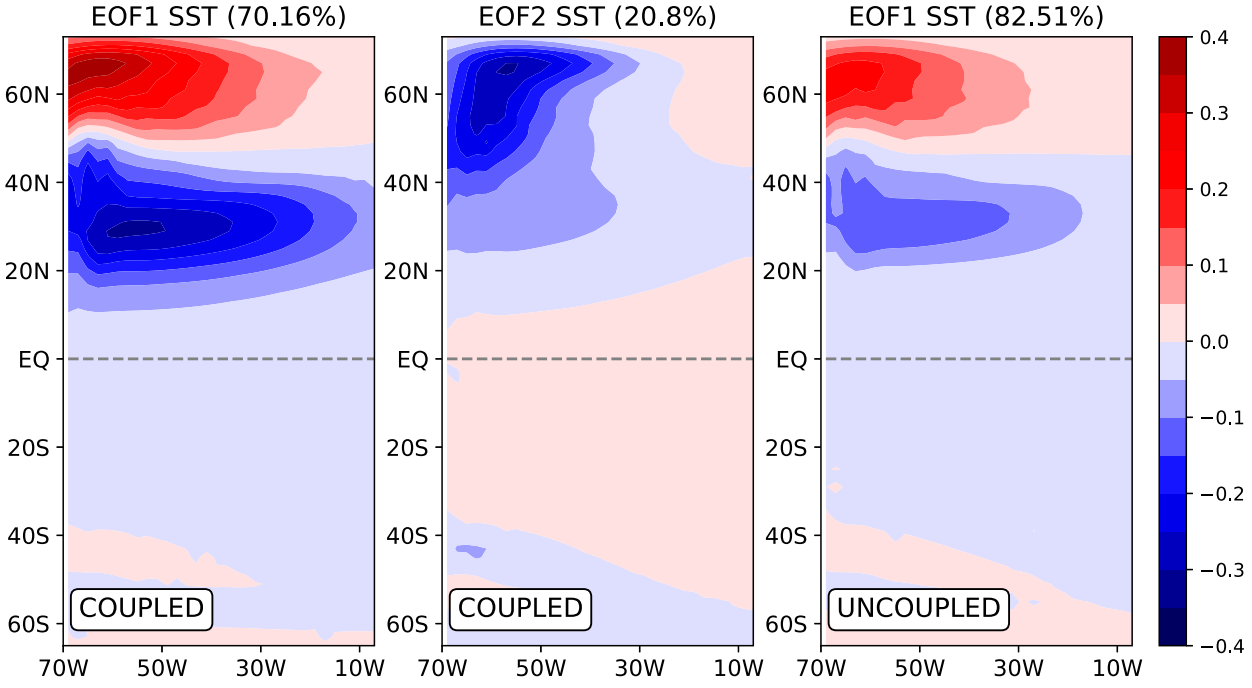

FIG. 8. Leading patterns of SST variability (°C) and explained variance (%) in the damped regime shown here for the specific diffusivity value $K = 1400\ \mathrm{m^2\ s^{-1}}$. Shown are the first two EOFs and the first EOF in the stochastic coupled and uncoupled systems, respectively.

Which of the ocean or atmosphere represents the major energy source for the variability? How does the contribution of the atmosphere and ocean to the production of temperature variance depend on thermal coupling and oceanic eddy diffusivities? To answer these questions, we now compute the ratio $R = S_O/(S_O + S_A^+)$, where $S_A^+ = S_A$ if $S_A > 0$ and is equal to 0 otherwise. This ratio thus provides the fraction of the production of buoyancy variance associated with S_O and S_A explained by internal ocean dynamics. If $S_A \leq 0$, then internal ocean dynamics (S_O) explains 100% of the production of the buoyancy variance associated with the ensemble S_O and S_A. The results are presented in Fig. 7d. Quite clearly the leading role of internal ocean dynamics in the variability extends beyond the supercritical regime to a much larger range of K values when thermal coupling with the atmosphere, as measured by the atmospheric feedback on SST anomalies, is enabled. Of course, stochastic forcing is required to generate variability in the damped regime, but the growth of upper-ocean heat content (250 m) anomalies is however mostly explained by changing ocean currents rather than by the direct thermodynamic response of the mixed layer to the noise forcing. Importantly this behavior occurs despite the fact that the leading pattern of the variability in the damped regime bears some resemblance to the imposed NAO forcing (Fig. 8). The imprint of the internal ocean mode in this damped regime is clearly seen in the second EOF of SST anomalies (Fig. 8), which appears to be similar to the leading pattern obtained in the supercritical regime (Fig. 5). We further note that the pattern correlation between the coupled and uncoupled systems in the damped regime is high (Fig. 8), a behavior that sharply contrasts with that obtained in the supercritical regime (Fig. 5). In the forced configuration, internal ocean dynamics is the primary driver of the upper-ocean heat content (0–250 m) variability for all values of K (Fig. 7d).

The results obtained here have been obtained using a very specific time scale of noise coherence of 10 days. Additional experiments not presented here reveal that increasing this time scale to 30 days has the effect of increasing the production of buoyancy variance by both surface fluxes (S_A) and internal ocean dynamics (S_O), the effect being much more pronounced in the damped regime. As a whole, the increase in S_A is larger than the increase in S_O, implying that a more coherent noise tends to increase (decrease) the role of the surface fluxes (internal ocean dynamics) in the variability. However, the ocean is still the dominant contributor to the growth of buoyancy variance in the northwestern corner of the basin and in the upper 250 m for diffusivity values up to $2200\ \mathrm{m^2\ s^{-1}}$ (not shown).

Figure 9 illustrates finally how the contribution of the ocean and atmosphere to the temperature variability of the coupled system changes as the averaging depth increases from 50 m (the depth of the forcing layer) to 1150 m (roughly the thermocline depth), with the 250-m averaging depth chosen previously being an intermediate value. Quite clearly the greater the averaging depth the stronger the contribution of internal ocean dynamics to the variability, irrespective of the values of K. For instance, changes in surface heat fluxes represent the leading energy source of the SST variability in the strongly damped regime, for $K > 1700\ \mathrm{m^2\ s^{-1}}$. Upper-ocean heat content variability (0–1150 m) in this range is however mostly constrained by the production of temperature variance associated with internal ocean dynamics. The reason for this behavior is

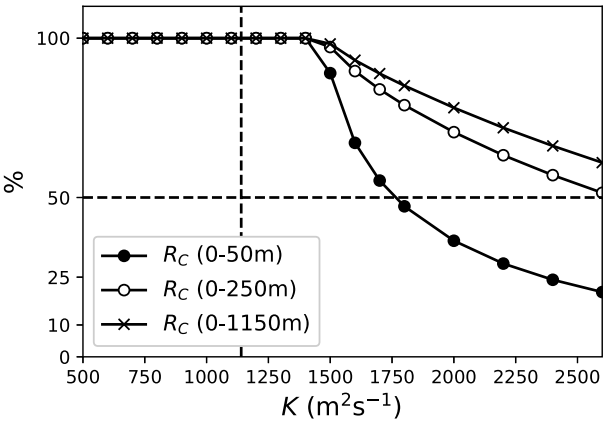

FIG. 9. Contribution $R = S_O/(S_O + S_A^+)$ (%; see text for details) of internal ocean dynamics to the production of buoyancy variance in the northwestern corner of the domain (46°–74°N, 70°–50°W) as a function of the horizontal diffusivity K. The calculation is done for the stochastic coupled (R_C) case only and in the upper 50, 250, and 1150 m. The vertical dashed (dotted) line indicates the corresponding position of the Hopf bifurcation at $K = 1140$ m^2 s^{-1} whereas the horizontal dashed line corresponds to the pivotal value where $S_A = S_O$.

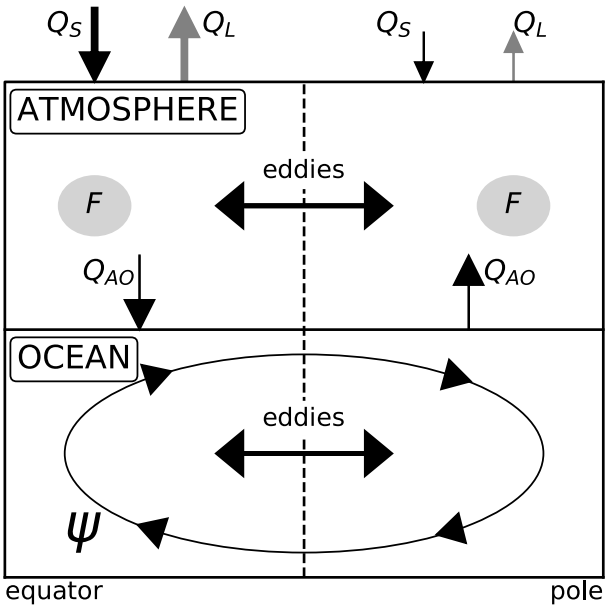

FIG. 10. Geometry of the single-hemisphere coupled ocean–atmosphere box model. Two oceanic boxes are coupled to two atmospheric boxes in the meridional plane. Radiative fluxes at the top of the atmosphere are the solar forcing Q_S and outgoing longwave radiation Q_L. The ocean and atmosphere exchange heat through turbulent sensible fluxes Q_{AO}. The term F acting on the atmospheric layer represents the dynamical part of the forcing and is taken to be stochastic. Mixing by turbulent motions between the tropical and polar boxes within the atmosphere and ocean is taken into account. Advective heat exchange between the two oceanic boxes is entirely accomplished by the meridional overturning circulation Ψ.

that the S_A term is only nonzero in the forcing layer (upper 50 m) whereas S_O monotonically decreases with depth, consistent with the result that the temperature anomalies mostly project onto the first baroclinic mode whose vertical extent is $\mathcal{O}(1000)$ m. Performing the variance budget over a greater depth has the effect of decreasing S_O but at a much lower rate than S_A, implying a greater role of internal ocean dynamics in the variability.

6. A coupled ocean–atmosphere box model

To better understand the way thermal coupling reinforces the internal oceanic contribution to the variability we propose herein a conceptual dynamical system with two degrees of freedom first introduced by Colin de Verdière and Huck (2000) to study interdecadal oscillations of the oceanic overturning under deterministic conditions. The strength of this conceptual model resides in the fact that it captures the behavior obtained in GCMs, and in particular the Hopf bifurcation at the transition between the steady and oscillatory regimes (Arzel et al. 2018). This model is modified here to include atmospheric stochastic forcing (Fig. 10).

a. Model description

A detailed derivation of the model from first principles can be found in the appendix. We simply provide here a brief description of the model and governing equations before going on to its analysis in the following sections. The model represents advection, dissipation and exchange of heat within and between the ocean and atmosphere in a single-hemisphere configuration (Fig. 10). The meridional redistribution of heat by advective processes between the tropical and polar boxes in the ocean is assumed to be entirely accomplished by the meridional overturning circulation. The oscillations we are studying here arise under constant surface wind stress forcing. As such, heat transport by the gyre circulation does not play a fundamental role in the variability and will therefore be discarded, as opposed for instance to Marshall et al. (2001). The overturning circulation is assumed to vary in quadrature with the anomalous temperature contrast, in agreement with results from previous studies (Huck et al. 1999a; te Raa and Dijkstra 2002). This feature is also clearly apparent here with the rate of change in the MOC being highly correlated ($r = 0.75$) with the anomalous SST contrast between the subtropics (20°–48°N) and the subpolar area (48°–74°N) in all model configurations, irrespective of the oceanic state being in the damped or supercritical regime. The time lag between meridional circulation anomalies and changes in the meridional temperature contrast represents the delay associated with westward-propagating planetary waves. Turbulent mixing by mesoscale eddies in the ocean and by synoptic-scale disturbances in the atmosphere between the tropical and polar boxes is included. Stochastic forcing is applied to the atmospheric layer with the same decorrelation time ($\tau_N = 10$ days) and amplitude ($\sigma_N = 100$ W m^{-2}) as the 3D model. Oceanic baroclinic instability is parameterized through a linear growth

rate μ for the strength of the meridional circulation. This parameter constitutes the most important parameter of the box model because it tells us whether the oceanic state belongs to the supercritical or damped regime depending on the choice of oceanic and atmospheric turbulent diffusivities and other thermal damping coefficients. A dynamical ocean is thus added in the simpler way to the Hasselmann (1976) formulation. The nondimensional model equations [Eqs. (A5) and (A7) in the appendix] are given by

$$\dot{x}' = -2\psi' - \delta x' + \beta N_0, \tag{10a}$$

$$\dot{\psi}' = \kappa x' + \mu\psi' - \gamma\psi'^3, \tag{10b}$$

where x' is the perturbation oceanic temperature difference between the tropical and polar boxes and ψ' the perturbation oceanic meridional overturning circulation. There is no evolution equation of the atmospheric temperature since on the long (decadal) time scales of interest here; the atmosphere is in instantaneous equilibrium with its fluxes. Under this approximation, the atmospheric temperature becomes diagnostic and the atmosphere enters the problem only through the parameters δ, β, and N_0. More specifically, δ sums up the oceanic and atmospheric contributions to oceanic thermal damping (oceanic and atmospheric eddy diffusivity, turbulent air–sea heat exchange, longwave radiative feedback) and β represents the amplitude of the atmospheric stochastic forcing N_0 seen by the ocean. The last cubic term has been introduced to stabilize the system at large amplitudes. We choose $\gamma = 300$ in all experiments. Following the previous approach, three different configurations of the box model impacting the coefficients δ and β are considered. The first one is the standard case where ocean-atmosphere thermal coupling is enabled, with coefficients

$$\delta = \alpha[2K_O + \lambda(1 - \sigma)] \quad \text{and} \quad \beta = \alpha\sigma\sigma_N/\overline{x} \tag{11}$$

with $\alpha = \tau/C_O$ and $\sigma = \lambda/(\lambda + B + 2K_A)$. Here $\tau = 1$ year is the scale for time, $C_O = 4 \times 10^9$ J K^{-1} m^{-2} is the heat capacity of the thermocline whose depth is fixed to 1000 m, $\overline{x} = 20$°C is the mean meridional temperature contrast between the tropical and polar boxes, $\lambda = 30$ W m^{-2} K^{-1} is the air–sea heat exchange coefficient, $K_O = 1$ W m^{-2} K^{-1} (corresponding to 1000 m^2 s^{-1}), $K_A = 2.275$ W m^{-2} K^{-1} is the atmospheric eddy diffusivity (corresponding to 1.3×10^6 m^2 s^{-1}), and $B = 1.7$ W m^{-2} K^{-1} is the longwave feedback at the top of the atmosphere. The second case is the forced ocean-only case, where

$$\delta = 2\alpha K_O \quad \text{and} \quad \beta = \alpha\sigma\sigma_N/\overline{x}. \tag{12}$$

The third case is the uncoupled one where the feedback of the atmosphere on oceanic temperature anomalies is suppressed where

$$\delta = \alpha(2K_O + \lambda) \quad \text{and} \quad \beta = \alpha\sigma\sigma_N/\overline{x}. \tag{13}$$

b. *Bifurcations, oscillation period, and power spectra*

Using the values of δ for the coupled, uncoupled, and forced cases, we see that as μ increases, oscillations first emerge in the forced case ($\mu_c = 0.016$), then in the coupled case ($\mu_c = 0.057$), and last in the uncoupled case ($\mu_c = 0.25$). The transition from the nonoscillatory to the oscillatory regime occurs through a genuine Hopf bifurcation (see the appendix for details). This sequence of bifurcations is presented in Fig. 11 for the amplitude of the changes in the meridional temperature contrast, as obtained from a 10 000-yr numerical integration of the box model. This sequence of bifurcations is consistent with the results from the 3D model (Fig. 6), demonstrating the relevance of this box model to study the physics of interdecadal oscillations of the overturning circulation and the effect of ocean–atmosphere thermal coupling, as we shall now see.

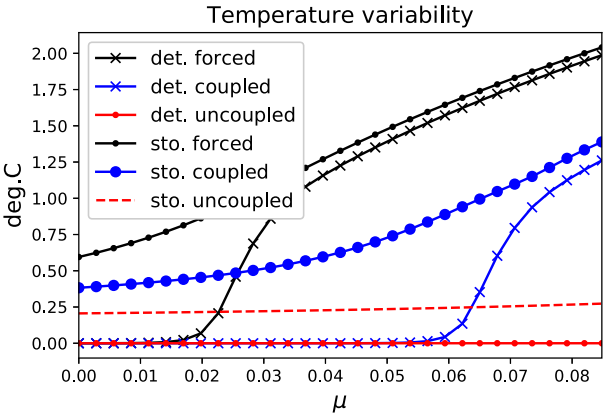

FIG. 11. Standard deviation of the anomalous meridional temperature contrast in the box model. For each value of the baroclinic growth rate μ, the coupled system is integrated for 10 000 years using a fourth-order Runge–Kutta scheme and the statistics are computed over the second half of the integration. The integration is done for the coupled, uncoupled, and forced cases under both deterministic and stochastic conditions. Hopf bifurcations occur successively at $\mu = 0.016$, 0.057, and 0.25 for the forced, coupled, and uncoupled cases. Over the range of values of μ considered here, the deterministic uncoupled system is always stable.

Figure 12 shows the theoretical power spectra [Eq. (A8) in the appendix] for the meridional temperature contrast at $\mu = 0$ for the coupled, uncoupled, and forced cases and for cases where the circulation is free to interact with the temperature field (solid lines) and prescribed to its background value (dashed lines). If the circulation is not allowed to vary, technically by setting $\psi' = 0$ in (10a), the canonical response of Hasselmann (1976) is obtained: a red spectrum at high frequencies that levels out when $\omega < \mu_c$. Circulation changes are thus essential in producing a preferred time scale in the system, consistent with realistic ocean-only simulations of the MITgcm (Arzel and Huck 2020). The effect of thermal coupling is to reduce the damping of oceanic temperature anomalies compared to the uncoupled case. There is therefore more variability in the coupled case compared to the uncoupled case. This result is independent of the circulation being prescribed or not. The forced response exhibits the highest variance since the damping of temperature anomalies is even weaker in this case, with an effective damping

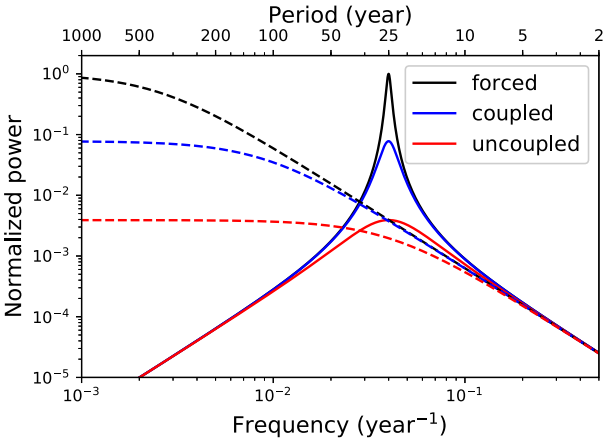

FIG. 12. Theoretical power spectra (A8) of temperature anomalies for $\mu = 0$ and for the coupled, uncoupled, and forced cases (solid lines). When circulation changes are inhibited ($\psi' = 0$), the canonical red noise response is obtained (dashed lines) with a temperature spectrum given by $|\hat{X}(\nu)|^2 = [\beta^2|\hat{N}(\nu)|^2]/(4\pi^2\nu^2 + \mu_c^2)$ All the spectra are normalized by the peak value of the forced case.

time scale $\tau\delta^{-1}$ of 63 years (compared to 18 and 4 years in the coupled and uncoupled cases respectively). These results are in good agreement with those deduced from the 3D model (Fig. 4).

c. *Energy sources*

Following previous studies and the present approach, insight into the physical mechanisms driving the variability can be obtained by multiplying the temperature equation by x' and averaging over a long time period (denoted by an overbar):

$$\frac{1}{2}\dot{\overline{x'^2}} = -2\overline{\psi' x'} + \beta\overline{x' N_0} - \delta\overline{x'^2}. \tag{14}$$

Similar to (9), the growth of temperature variance can originate either from internal ocean dynamics ($-2\overline{\psi' x'}$) or from the direct effect of stochastic forcing on the oceanic temperature ($\beta\overline{x' N_0}$). The last term is always negative and represents a sink of temperature variance. The results for the coupled and uncoupled cases are presented in Fig. 13. As can be seen the box model reproduces with very high fidelity the results obtained with the full 3D model (Fig. 7). The major points are that thermal coupling 1) significantly increases the production of temperature variance by internal oceanic processes; 2) significantly increases the destruction of temperature variance by air–sea heat fluxes, except in the most weakly unstable cases where the effect of coupling is to reinforce the production of temperature variance by air–sea heat fluxes; and 3) as a whole significantly reinforces the role of internal ocean dynamics in the variability, in particular in the damped regime.

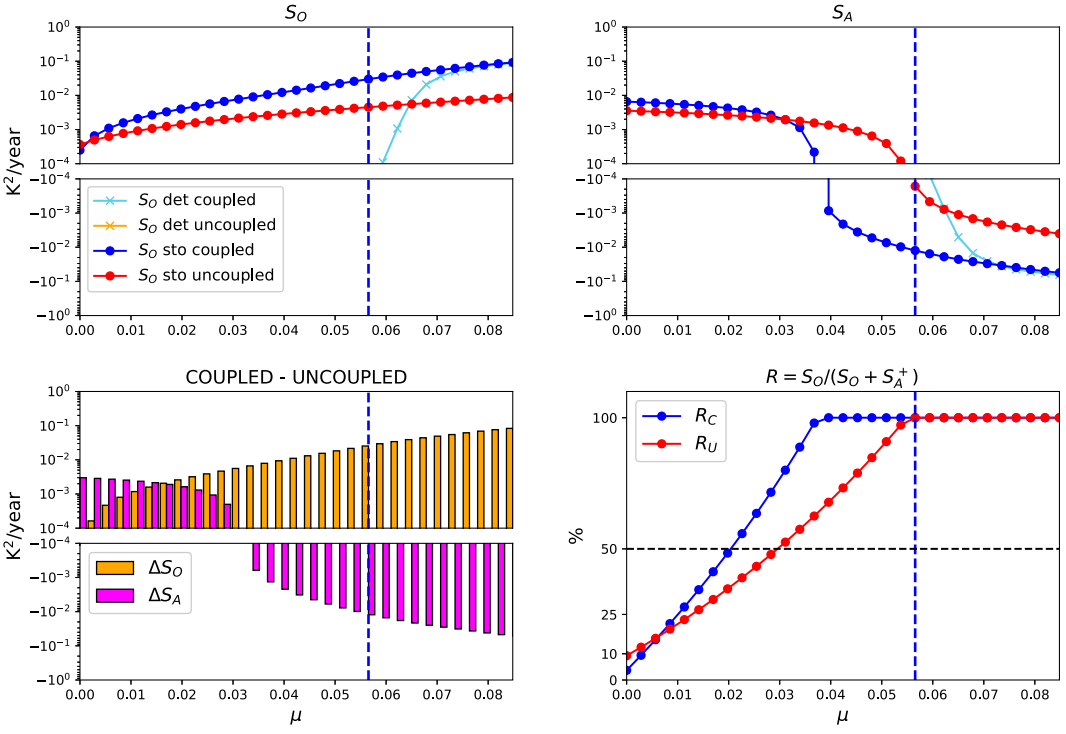

FIG. 13. Temperature variance budget in the coupled ocean–atmosphere box model, as obtained from a 10 000-yr-long numerical integration. Shown are the oceanic ($S_O = -2\overline{x'\Psi'}$) and atmospheric energy source ($S_A = \beta\overline{x' N_0}$) terms for both the coupled and uncoupled systems under both deterministic and stochastic forcing conditions as a function of the growth rate μ, the differences in S_O and S_A between the coupled and uncoupled systems and the ratio $R = S_O/(S_O + S_A^+)$ measuring the fraction of the total production of temperature variance explained by internal ocean dynamics. In the calculation of R only positive values of S_A are retained so that $S_A^+ = 0$ wherever $S_A < 0$.

7. Summary and discussion

The impact of ocean–atmosphere thermal coupling, as measured by the atmospheric feedback on SST anomalies, on the primary drivers of interdecadal variability has been investigated using an idealized coupled model. The main advantage of such a model is its ability to explore a greater parameter regime than that would be possible with a comprehensive coupled GCM. The effect of thermal coupling on the primary drivers of the variability was quantified across a wide range of oceanic eddy diffusivities from a comparison of the buoyancy variance budget of coupled and uncoupled integrations.

The results first confirm that the primary effect of thermal coupling is to reduce the internal damping of temperature anomalies due to surface heat fluxes (Barsugli and Battisti 1998). This reduced damping leads to a greater thermal variance in both the ocean and atmosphere as well as greater ocean circulation changes in coupled integrations compared to uncoupled ones, in agreement with Wu and Liu (2005). One new aspect is that the amplifying effect of thermal coupling on the variability is much stronger in the supercritical than in the damped regime. The presence of an internal ocean mode in the supercritical regime therefore provides a significant positive feedback on the amplitude of the variability through reduced thermal damping by surface heat fluxes. Thermal coupling is also shown to significantly alter the spatial pattern of the variability, in particular in the supercritical regime. When the interdecadal internal ocean mode is damped, however, the pattern correlation between the coupled and uncoupled leading EOFs is large. The analysis presented by Wu and Liu (2005) falls within this latter regime, suggesting that the internal ocean mode in their model is damped.

The buoyancy variance budget then reveals that internal ocean dynamics always acts as a source of temperature variance, irrespective of the coupling with the atmosphere being present or not or the oceanic state being in the supercritical or damped regimes. On the contrary changes in surface buoyancy fluxes always act to damp the variability in the supercritical regime. Only for the most diffusive, weakly unstable states does the atmosphere act as a source of energy for the variability through the stochastic forcing exceeding surface heat flux damping. These behaviors are present in both the coupled and uncoupled configurations of the model, but with different magnitudes. Overall thermal coupling with the atmosphere is shown to significantly reinforce the role of internal ocean dynamics in the interdecadal variability of the coupled ocean–atmosphere system, particularly in the damped regime. This result constitutes the major finding of our study. Specifically, it is shown that the leading role of internal ocean dynamics in the variability extends beyond the supercritical regime to a much larger range of diffusivity values when thermal coupling with the atmosphere is enabled. Put another way, thermal coupling with the atmosphere significantly widens the range of diffusivity values over which internal ocean dynamics drives the variability. Of course, stochastic forcing is required to generate variability in the damped regime. The growth of upper-ocean heat content anomalies in this regime is, however, mostly constrained by changing ocean currents associated with the noise excitation of the internal ocean mode rather than by the direct thermodynamic response of the mixed layer to the noise forcing. Importantly this behavior occurs despite the fact that the leading pattern of the variability in the damped regime bears some resemblance to the imposed NAO forcing. The same conclusion applies to the underlying mechanism driving interdecadal sea surface temperature variability. These results are in line with the more general statement that the ocean drives the midlatitude North Atlantic variability on decadal and longer time scales (Bjerknes 1964; Gulev et al. 2013; O'Reilly et al. 2016; Garuba et al. 2018).

A stochastic coupled ocean–atmosphere model is finally proposed that captures the basic effect of ocean–atmosphere thermal coupling, as obtained in the 3D model. The box model builds upon a stochastically forced atmospheric component coupled to a dynamical ocean. The presence of the latter significantly modifies the response of the coupled system to stochastic forcing, first by introducing an additional and significant source of temperature variance in the system, and second by selecting an interdecadal time scale as opposed to pure thermodynamic models (Hasselmann 1976; Barsugli and Battisti 1998; Clement et al. 2016). The fact that the effect of coupling is captured by a simple 2-degree-of-freedom dynamical system suggests that the proposed mechanism does not depend on the details of the 3D model and is therefore a robust feature of the ocean–atmosphere system.

There are, of course, several fundamental aspects of the real climate system that are missing from our idealized framework. Perhaps the most critical is the absence of a dynamical atmospheric component. With a full dynamical atmosphere, NAO related stochastic forcing would adjust its amplitude and spatial pattern to the changing ocean surface conditions and feed back onto the SST field such that coupled air–sea modes or resonant behaviors could emerge (Weaver and Valcke 1998; Wu and Liu 2005; Ortega et al. 2015). The absence of a seasonal cycle and the limited poleward extent of the ocean domain does not allow the emergence of sea ice although a simple one-layer thermodynamic sea ice component identical to that used by Colin de Verdière and Te Raa (2010) is present. The variability studied here is typically enhanced at midlatitudes along the North Atlantic Current (Ortega et al. 2015; Arzel et al. 2018; Gastineau et al. 2018; Arzel and Huck 2020) so that direct sea ice effects are unimportant. It would however be interesting to assess the effect of thermal coupling on the variability of coupled climate models presenting a source of variability related to Arctic–Atlantic interactions (Jungclaus et al. 2005; Escudier et al. 2013). Studies using idealized ocean models such as the present one showed that the presence of ocean bathymetry, absent here, may partially (Buckley et al. 2012) or completely damp out (Winton 1997) intrinsic interdecadal ocean modes. Such contrasting behaviors suggest that the details of the model configuration and choice of forcing/parameters are critical in determining the response of the variability to the presence of bathymetry. Arzel et al. (2018) showed that the internal ocean variability studied here and also previously (Colin de Verdière and Huck 1999; te Raa et al. 2004; Buckley et al. 2012) exists for some

parameter range in a global configuration of the MITgcm, including realistic continental geometry and ocean bathymetry. Although ocean bathymetry clearly impacts the mode characteristics (period and spatial pattern) as shown by te Raa et al. (2004), it does not modify the generic large-scale baroclinic instability mechanism at the heart of the internal ocean variability. The lack of oceanic turbulence is another limitation of our model. With resolved mesoscale eddies the explicit horizontal diffusivity used here becomes irrelevant and another critical parameter, such as vertical diffusivity used by Farneti and Vallis (2011) for instance, would be required to explore the physics of the variability in both the damped and supercritical regimes. The presence of oceanic mesoscale eddies does not modify the generic mechanism of baroclinic instability captured in our simple model (Huck et al. 2015), but simply acts as a sink of temperature variance at interdecadal time scales (Hochet et al. 2020, 2022). As such the leading role of internal ocean dynamics in the variability advocated in the present study is probably overestimated compared to a situation where mesoscale eddies are resolved. Additional studies based on strongly eddying quasigeostrophic coupled models point to a strong coupling between the ocean and atmosphere on decadal and longer time scales (Kravtsov et al. 2007; Martin et al. 2021). These quasigeostrophic models cannot capture the large-scale baroclinic instability mechanism that is at play in our model, because it develops in regions of steep isopycnal slopes. Future work based on primitive ocean models at eddying resolutions will need to be pursued to assess which mechanism among the few listed here is the most relevant for driving temperature variance from midlatitudes to subpolar latitudes as well as the role of thermal coupling, which is still debated (e.g., Weaver and Valcke 1998; Timmermann et al. 1998; Delworth and Greatbatch 2000; Dong and Sutton 2005; Gastineau et al. 2018). The generic large-scale baroclinic instability mechanism driving internal oceanic variability in the planetary geostrophic ocean component of the present model (Colin de Verdière and Huck 1999; Huck et al. 2001) has been shown to be robust in comprehensive ocean climate models (Sévellec and Fedorov 2013; Ortega et al. 2015; Arzel et al. 2018; Gastineau et al. 2018). We thus feel confident that the mechanisms presented here might play a role in more realistic contexts. As a final note we wish to stress the extreme usefulness of the buoyancy variance budget combined with the coupled/uncoupled modeling approach to identify the primary drivers of the variability and unravel the role of thermal coupling. Applying such a budget in coupled and uncoupled configurations of comprehensive GCMs and realistic climate models will undoubtedly improve our understanding of the mechanisms driving climate variability on interdecadal time scales in those models.

Acknowledgments. We thank the three anonymous reviewers and the editor Robert C. J. Wills for their valuable comments and suggestions that helped improve the manuscript. We are grateful to Alain Colin de Verdière, who provided helpful criticism on an early version of this manuscript. The authors acknowledge the Pôle de Calcul et de Données Marines (PCDM at IFREMER, Brest) for providing DATARMOR computational resources.

Data availability statement. The data that support the findings of this study are stored on IFREMER (Brest, France) servers and can be made available upon reasonable request to the corresponding author.

APPENDIX

The Coupled Ocean–Atmosphere Box Model

a. Model equations

Radiative imbalance at the top of the atmosphere (Fig. 10) arises due to differences between incoming solar flux Q_S (assumed constant) and outgoing longwave radiation Q_L, which is linearized around the atmospheric temperature T_a (i.e., $Q_L = A + BT_a$). The term F acting on the atmospheric layer represents the dynamical part of the forcing, which is taken to be stochastic. The turbulent surface heat flux Q_{AO} (assumed positive downward) between the ocean and atmosphere is equal to $\lambda(T_a - T_o)$, where λ is the air–sea heat exchange coefficient and T_o is the oceanic temperature. Using $\lambda = 30$ W m^{-2} K^{-1}, an atmospheric heat capacity $C_a = \rho_a C_{pa} h_a = 7 \times 10^6$ J m^{-2} K^{-1} (assuming an atmospheric scale height $h_a = 7$ km, and standard values for air density ρ_a and specific heat capacity of air C_{pa}), we obtain an atmospheric damping time scale C_a/λ of $\mathcal{O}(1)$ day. Since we are interested in time scales of the order of 10 years or longer, it is legitimate to assume that the atmosphere is in instantaneous equilibrium with the ocean and the stochastic forcing (Saravanan and McWilliams 1998). The heat budget of the atmospheric box i then reads

$$Q_S^i - Q_L^i - Q_{ao}^i + K_A(T_a^j - T_a^i) + F^i = 0, \tag{A1}$$

where $j = 3 - i$ and K_A parameterizes the turbulent heat exchange by large-scale atmospheric eddies between the tropical ($i = 1$) and the polar ($i = 2$) boxes. The heat budget of the oceanic box i is

$$C_O \frac{\partial T^i}{\partial t} = Q_{ao}^i + \frac{C_O}{a_i}\psi(T^j - T^i) + K_O(T^j - T^i), \tag{A2}$$

where ψ (m^3 s^{-1}) is the overturning strength; $C_O = \rho_o C_{po} h$ is the heat capacity of the ocean where ρ_o, C_{po}, and h are the density, specific heat of water, and ocean depth, respectively; and K_O parameterizes the turbulent heat exchange by mesoscale eddies between the two oceanic boxes. Following Colin de Verdière and Huck (2000) we concentrate on the variability of the temperature differences between the two boxes. Introducing $x = T^1 - T^2$ for the ocean and $y = T_A^1 - T_A^2$ for the atmosphere and assuming equal areas a_i ($a_i = a = 4 \times 10^6$ km^2) for the two boxes allows us to write

$$S - By - \lambda(y - x) - 2K_A y + N = 0 \tag{A3}$$

and

$$\dot{x} = \alpha\lambda(y - x) - 2\psi x - 2K_O \alpha x, \tag{A4}$$

where $\alpha = \tau/C_O$ and ψ is scaled by ha/τ where $\tau = 1$ year. The terms S and N are the differences of solar flux and

noise forcing between the tropical and polar boxes respectively. The noise forcing is written as $N = \sigma_N N_0$, where σ_N is the amplitude of the forcing and N_0 obeys a first-order autoregressive process with standard deviation equal to 1 and decorrelation time $\tau_N = 10$ days. Linearizing now the thermodynamic equations, Eqs. (A3) and (A4), around a time mean state (denoted by an overbar), substituting (A3) into (A4), and nondimensionalizing the oceanic temperature anomaly x' by $\bar{x}$ the mean meridional temperature contrast, we obtain

$$\dot{x}' = -2\psi' - \delta x' + \beta N_0, \tag{A5}$$

where ψ' is the anomalous overturning circulation. It has been shown from 3D numerical experiments (Huck et al. 1999a) that temperature anomalies are mostly constrained by anomalous advection rather than mean flow effects. Hence the term $-2\bar{\psi}x'$ is neglected. The coefficients δ and β are given by

$$\delta = \alpha[2K_O + \lambda(1 - \sigma)] \quad \text{and} \quad \beta = \alpha\sigma\sigma_N/\bar{x}, \tag{A6}$$

with $\sigma = \lambda/(\lambda + B + 2K_A)$. Using $B = 1.7$ W m^{-2} K^{-1}, $K_A = 2.275$ W m^{-2} K^{-1} (equivalent to an atmospheric eddy diffusivity $K_A \times a/C_a = 1.3 \times 10^6$ m^2 s^{-1}), and $K_O = 1$ W m^{-2} K^{-1} (equivalent to an oceanic eddy diffusivity of $K_O \times a/C_O = 1000$ m^2 s^{-1}, with $C_O = 4 \times 10^9$ J m^{-2} K^{-1}, for a 1000-m ocean depth), we obtain a damping time scale $\tau\delta^{-1}$ of oceanic temperature anomalies of about 18 years. This time scale is much longer than the typical e-folding times of $\mathcal{O}(1)$ year of unstable planetary waves computed from OGCM studies (Arzel et al. 2018) suggesting the potential for spontaneous oscillations developing in ocean-only integrations to survive to coupling with the atmosphere. Notice that the magnitude of the noise forcing seen by the ocean is proportional to σ, which decreases with decreasing λ values and increasing K_A values. To close the system, an equation for the anomaly in the strength of the circulation is needed. With an attempt to encapsulate the ideas developed in the previous sections, at least two features must be represented. The first one is the baroclinic instability mechanism, which is parameterized here through the use of a linear growth rate μ. The second one is the apparent phase lag that exists between the meridional temperature gradient and the MOC. These aspects encourage us to follow Colin de Verdière and Huck (2000) and use the same dynamics, that is,

$$\dot{\psi}' = \kappa x' + \mu\psi' - \gamma\psi'^3, \tag{A7}$$

where the last cubic term has been introduced to stabilize the system at large amplitudes. The sensitivity of model solutions is studied in terms of the baroclinic growth rate μ.

b. Properties of the solutions

In the deterministic case ($\beta = 0$) and in the small amplitude limit, it can easily be shown (Colin de Verdière and Huck 2000) that the eigensolutions are unstable for $\mu > \mu_c = \delta$ provided that $\delta < \sqrt{2\kappa}$. At $\mu = \mu_c$ a supercritical Hopf bifurcation occurs. Physically this means that when the growth rate of perturbations becomes larger than all sources of thermal damping, the oscillations can grow and eventually settle into a finite amplitude limit cycle. In the stochastic regime, the statistics of the variability can be deduced from the temperature spectra in the small-amplitude limit:

$$|\hat{X}(\omega)|^2 = \frac{\beta^2|\hat{N}_0(\omega)|^2}{\omega^2 a(\omega)^2 + b(\omega)^2}, \tag{A8}$$

where $\hat{N}_0(\omega)$ is the Fourier transform of the noise forcing and

$$a(\omega) = 1 - \frac{2\kappa}{\omega^2 + \mu^2} \quad \text{and} \tag{A9a}$$

$$b(\omega) = \mu_c - \frac{2\kappa\mu}{\omega^2 + \mu^2}. \tag{A9b}$$

For time scales much longer than $\mathcal{O}(10)$ days, the stochastic forcing is essentially white and $\hat{N}_0(\omega) = 1$. In this case an analytical expression for the most energetic time scale $T_0 = 2\pi\omega_0^{-1}$ of the variability can be deduced from (A8) and will be valid as long as it is much longer than the atmospheric spindown time scale,

$$T_0 = 2\pi\left[2\sqrt{\kappa}(\mu^2 - \mu\mu_c + \kappa)^{1/2} - \mu^2\right]^{-1/2}, \tag{A10}$$

while the amplitude of temperature variations is given by $[\int|\hat{X}(\omega)|^2 d\omega]^{1/2}$. With $\kappa = 0.0315$, a period of 25 years is obtained in the coupled, uncoupled, and forced cases, similar to the 3D model. It is readily seen that the period in the deterministic case $2\pi[2\kappa - (\mu + \mu_c)^2/4]^{-1/2}$ closely follows that obtained under stochastic forcing as long as $\mu < \mu_c \ll 1$. At bifurcation $\mu = \mu_c$ the period of the variability predicted by the deterministic solution is exactly recovered by (A10) but the linear assumption breaks down since $|\hat{X}(\omega_0)^2|$ becomes infinite. The stochastic linear solutions become invalid when approaching the Hopf bifurcation and are mostly useful in the most diffusive, weakly unstable cases where $\mu \ll \mu_c$.

REFERENCES

Abernathey, R. P., and J. Marshall, 2013: Global surface eddy diffusivities derived from satellite altimetry. *J. Geophys. Res. Oceans*, **118**, 901–916, https://doi.org/10.1002/jgrc.20066.

Arzel, O., and T. Huck, 2020: Contributions of atmospheric stochastic forcing and intrinsic ocean modes to North Atlantic Ocean interdecadal variability. *J. Climate*, **33**, 2351–2370, https://doi.org/10.1175/JCLI-D-19-0522.1.

——, ——, and A. Colin de Verdière, 2006: The different nature of interdecadal variability of the thermohaline circulation under mixed and flux boundary conditions. *J. Phys. Oceanogr.*, **36**, 1703–1718, https://doi.org/10.1175/JPO2938.1.

——, A. Colin de Verdière, and T. Huck, 2007: On the origin of interdecadal oscillations in a coupled ocean–atmosphere model. *Tellus*, **59**, 367–383, https://doi.org/10.1111/j.1600-0870.2007.00227.x.

——, M. H. England, A. Colin de Verdière, and T. Huck, 2012: Abrupt millennial variability and interdecadal-interstadial oscillations in a global coupled model: Sensitivity to the background climate state. *Climate Dyn.*, **39**, 259–275, https://doi.org/10.1007/s00382-011-1117-y.

——, T. Huck, and A. Colin de Verdière, 2018: The internal generation of the Atlantic Ocean interdecadal variability. *J. Climate*, **31**, 6411–6432, https://doi.org/10.1175/JCLI-D-17-0884.1.

Barsugli, J. J., and D. S. Battisti, 1998: The basic effects of atmosphere–ocean thermal coupling on midlatitude variability. *J. Atmos. Sci.*, **55**, 477–493, https://doi.org/10.1175/1520-0469(1998)055<0477:TBEOAO>2.0.CO;2.

Bjerknes, J., 1964: Atlantic air–sea interaction. *Advances in Geophysics*, Vol. 10, Academic Press, 1–82, https://doi.org/10.1016/S0065-2687(08)60005-9.

Buckley, M. W., D. Ferreira, J.-M. Campin, J. Marshall, and R. Tulloch, 2012: On the relationship between decadal buoyancy anomalies and variability of the Atlantic meridional overturning circulation. *J. Climate*, **25**, 8009–8030, https://doi.org/10.1175/JCLI-D-11-00505.1.

Chen, F., and M. Ghil, 1996: Interdecadal variability in a hybrid coupled ocean–atmosphere model. *J. Phys. Oceanogr.*, **26**, 1561–1578, https://doi.org/10.1175/1520-0485(1996)026<1561:IVIAHC>2.0.CO;2.

Chylek, P., C. K. Folland, H. A. Dijkstra, G. Lesins, and M. K. Dubey, 2011: Ice-core data evidence for a prominent near 20 year time-scale of the Atlantic multidecadal oscillation. *Geophys. Res. Lett.*, **38**, L13704, https://doi.org/10.1029/2011GL047501.

Clement, A., K. Bellomo, L. N. Murphy, M. A. Cane, T. Mauritsen, G. Radel, and B. Stevens, 2015: The Atlantic multidecadal oscillation without a role for ocean circulation. *Science*, **350**, 320–324, https://doi.org/10.1126/science.aab3980.

——, M. A. Cane, L. N. Murphy, K. Bellomo, T. Mauritsen, and B. Stevens, 2016: Response to comment on "The Atlantic multidecadal oscillation without a role for ocean circulation." *Science*, **352**, 1527, https://doi.org/10.1126/science.aaf2575.

Colin de Verdière, A., 1988: Buoyancy driven planetary flows. *J. Mar. Res.*, **46**, 215–265, https://doi.org/10.1357/002224088785113667.

——, and T. Huck, 1999: Baroclinic instability: An oceanic wavemaker for interdecadal variability. *J. Phys. Oceanogr.*, **29**, 893–910, https://doi.org/10.1175/1520-0485(1999)029<0893:BIAOWF>2.0.CO;2.

——, and ——, 2000: A 2 degree of freedom dynamical system for interdecadal oscillations of the ocean–atmosphere. *J. Climate*, **13**, 2801–2817, https://doi.org/10.1175/1520-0442(2000)013<2801:ADOFDS>2.0.CO;2.

——, and L. Te Raa, 2010: Weak oceanic heat transport as a cause of the instability of glacial climates. *Climate Dyn.*, **35**, 1237–1256, https://doi.org/10.1007/s00382-009-0675-8.

——, T. Meunier, and M. Ollitrault, 2019: Meridional overturning and heat transport from Argo floats displacements and the Planetary Geostrophic Method (PGM): Application to the subpolar North Atlantic. *J. Geophys. Res. Oceans*, **124**, 6270–6285, https://doi.org/10.1029/2018JC014565.

Delworth, T. L., and R. J. Greatbatch, 2000: Multidecadal thermohaline circulation variability excited by atmospheric surface flux forcing. *J. Climate*, **13**, 1481–1495, https://doi.org/10.1175/1520-0442(2000)013<1481:MTCVDB>2.0.CO;2.

——, R. Zhang, and M. E. Mann, 2007: Decadal to centennial variability of the Atlantic from observations and models. *Geophys. Monogr.*, Vol. 173, Amer. Geophys. Union, 131–148.

Deser, C., M. A. Alexander, S.-P. Xie, and A. S. Phillips, 2010: Sea surface temperature variability: Patterns and mechanisms. *Annu. Rev. Mar. Sci.*, **2**, 115–143, https://doi.org/10.1146/annurev-marine-120408-151453.

Dong, B., and R. T. Sutton, 2005: Mechanism of interdecadal thermohaline circulation variability in a coupled ocean–atmosphere GCM. *J. Climate*, **18**, 1117–1135, https://doi.org/10.1175/JCLI3328.1.

Escudier, R., J. Mignot, and D. Swingedouw, 2013: A 20-year coupled ocean–sea ice–atmosphere variability mode in the North Atlantic in an AOGCM. *Climate Dyn.*, **40**, 619–636, https://doi.org/10.1007/s00382-012-1402-4.

Fanning, A. F., and A. J. Weaver, 1996: An atmospheric energy-moisture balance model: Climatology, interpentadal climate change, and coupling to an ocean general circulation model. *J. Geophys. Res.*, **101**, 15 111–15 128, https://doi.org/10.1029/96JD01017.

Farneti, R., and G. K. Vallis, 2011: Mechanisms of interdecadal climate variability and the role of ocean–atmosphere coupling. *Climate Dyn.*, **36**, 289–308, https://doi.org/10.1007/s00382-009-0674-9.

Feldstein, S. B., 2000: The timescale, power spectra, and climate noise properties of teleconnection patterns. *J. Climate*, **13**, 4430–4440, https://doi.org/10.1175/1520-0442(2000)013<4430:TTPSAC>2.0.CO;2.

Frankcombe, L. M., and H. A. Dijkstra, 2009: Coherent multidecadal variability in North Atlantic sea level. *Geophys. Res. Lett.*, **36**, L15604, https://doi.org/10.1029/2009GL039455.

Garuba, O. A., J. Lu, H. A. Singh, F. Liu, and P. Rasch, 2018: On the relative roles of the atmosphere and ocean in the Atlantic multidecadal variability. *Geophys. Res. Lett.*, **45**, 9186–9196, https://doi.org/10.1029/2018GL078882.

Gastineau, G., J. Mignot, O. Arzel, and T. Huck, 2018: North Atlantic Ocean internal decadal variability: Role of the mean state and ocean–atmosphere coupling. *J. Geophys. Res. Oceans*, **123**, 5949–5970, https://doi.org/10.1029/2018JC014074.

Graves, C. E., W.-H. Lee, and G. R. North, 1993: New parametrizations and sensitivities for simple climate models. *J. Geophys. Res.*, **98**, 5025–5036, https://doi.org/10.1029/92JD02666.

Gray, S., L. Graumlich, J. Betancourt, and G. Pederson, 2004: A tree-ring based reconstruction of the Atlantic multidecadal oscillation since 1567 AD. *Geophys. Res. Lett.*, **31**, L12205, https://doi.org/10.1029/2004GL019932.

Greatbatch, R. J., and S. Zhang, 1995: An interdecadal oscillation in an idealized ocean basin forced by constant heat flux. *J. Climate*, **8**, 81–91, https://doi.org/10.1175/1520-0442(1995)008<0081:AIOIAI>2.0.CO;2.

Gulev, S. K., M. Latif, N. Keenlyside, W. Park, and K. P. Koltermann, 2013: North Atlantic Ocean control on surface heat flux on multidecadal timescales. *Nature*, **499**, 464–467, https://doi.org/10.1038/nature12268.

Hasselmann, K., 1976: Stochastic climate models. Part I: Theory. *Tellus*, **28**, 473–484, https://doi.org/10.3402/tellusa.v28i6.11316.

Held, I. M., 2005: The gap between simulating and understanding in climate modeling. *Bull. Amer. Meteor. Soc.*, **86**, 1609–1614, https://doi.org/10.1175/BAMS-86-11-1609.

Herbaut, C., J. Sirven, and S. Février, 2002: Response of a simplified oceanic general circulation model to idealized NAO-like stochastic forcing. *J. Phys. Oceanogr.*, **32**, 3182–3192, https://doi.org/10.1175/1520-0485(2002)032<3182:ROASOG>2.0.CO;2.

Hochet, A., T. Huck, O. Arzel, F. Sévellec, A. C. de Verdière, M. Mazloff, and B. Cornuelle, 2020: Direct temporal cascade of temperature variance in eddy-permitting simulations of

multidecadal variability. *J. Climate*, **33**, 9409–9425, https://doi.org/10.1175/JCLI-D-19-0921.1.

——, ——, ——, ——, and ——, 2022: Energy transfers between multidecadal and turbulent variability. *J. Climate*, **35**, 1157–1178, https://doi.org/10.1175/JCLI-D-21-0136.1.

Huang, R. X., 1998: Mixing and available potential energy in a Boussinesq ocean. *J. Phys. Oceanogr.*, **28**, 669–678, https://doi.org/10.1175/1520-0485(1998)028<0669:MAAPEI>2.0.CO;2.

Huck, T., A. Colin de Verdière, and A. Weaver, 1999a: Interdecadal variability of the thermohaline circulation in box-ocean models forced by fixed surface fluxes. *J. Phys. Oceanogr.*, **29**, 865–892, https://doi.org/10.1175/1520-0485(1999)029<0865:IVOTTC>2.0.CO;2.

——, A. J. Weaver, and A. Colin de Verdière, 1999b: On the influence of the parametrization of lateral boundary layers on the thermohaline circulation in coarse resolution ocean-models. *J. Mar. Res.*, **57**, 387–426, https://doi.org/10.1357/002224099764805138.

——, G. Vallis, and A. Colin de Verdière, 2001: On the robustness of the interdecadal modes of the thermohaline circulation. *J. Climate*, **14**, 940–963, https://doi.org/10.1175/1520-0442(2001)014<0940:OTROTI>2.0.CO;2.

——, O. Arzel, and F. Sévellec, 2015: Multidecadal variability of the overturning circulation in presence of eddy turbulence. *J. Phys. Oceanogr.*, **45**, 157–173, https://doi.org/10.1175/JPO-D-14-0114.1.

Jamet, Q., T. Huck, O. Arzel, J.-M. Campin, and A. Colin de Verdière, 2016: Oceanic control of multidecadal variability in an idealized coupled GCM. *Climate Dyn.*, **46**, 3079–3095, https://doi.org/10.1007/s00382-015-2754-3.

Jungclaus, J. H., H. Haak, M. Latif, and U. Mikolajewicz, 2005: Arctic–North Atlantic interactions and multidecadal variability of the meridional overturning circulation. *J. Climate*, **18**, 4013–4031, https://doi.org/10.1175/JCLI3462.1.

Kravtsov, S., W. K. Dewar, P. Berloff, J. C. McWilliams, and M. Ghil, 2007: A highly nonlinear coupled mode of decadal variability in a mid-latitude ocean–atmosphere model. *Dyn. Atmos. Oceans*, **43**, 123–150, https://doi.org/10.1016/j.dynatmoce.2006.08.001.

Mann, M. E., R. S. Bradley, and M. K. Hughes, 1998: Global-scale temperature patterns and climate forcing over the past six centuries. *Nature*, **392**, 779–787, https://doi.org/10.1038/33859.

——, B. A. Steinman, D. J. Brouillette, and S. K. Miller, 2021: Multidecadal climate oscillations during the past millennium driven by volcanic forcing. *Science*, **371**, 1014–1019, https://doi.org/10.1126/science.abc5810.

Marshall, J., and Coauthors, 2001: North Atlantic climate variability: Phenomena, impacts and mechanisms. *Int. J. Climatol.*, **21**, 1863–1898, https://doi.org/10.1002/joc.693.

——, J. R. Scott, A. Romanou, M. Kelley, and A. Leboissetier, 2017: The dependence of the ocean's MOC on mesoscale eddy diffusivities: A model study. *Ocean Modell.*, **111**, 1–8, https://doi.org/10.1016/j.ocemod.2017.01.001.

Martin, P. E., B. K. Arbic, and A. M. Hogg, 2021: Drivers of atmospheric and oceanic surface temperature variance: A frequency domain approach. *J. Climate*, **34**, 3975–3990, https://doi.org/10.1175/JCLI-D-20-0557.1.

Muir, M. C., and A. Fedorov, 2017: Evidence for the AMOC interdecadal mode related to westward propagation of temperature anomalies in CMIP5 models. *Climate Dyn.*, **48**, 1517–1535, https://doi.org/10.1007/s00382-016-3157-9.

Munk, W., and C. Wunsch, 1998: Abyssal recipes II: Energetics of tidal and wind mixing. *Deep-Sea Res. I*, **45**, 1977–2010, https://doi.org/10.1016/S0967-0637(98)00070-3.

North, G. R., R. F. Cahalan, and J. A. Coakley Jr., 1981: Energy balance climate models. *Rev. Geophys. Space Phys.*, **19**, 91–121, https://doi.org/10.1029/RG019i001p00091.

O'Reilly, C. H., M. Huber, T. Woollings, and L. Zanna, 2016: The signature of low-frequency oceanic forcing in the Atlantic multidecadal oscillation. *Geophys. Res. Lett.*, **43**, 2810–2818, https://doi.org/10.1002/2016GL067925.

Ortega, P., J. Mignot, D. Swingedouw, F. Sévellec, and E. Guilyardi, 2015: Reconciling two alternative mechanisms behind bi-decadal variability in the North Atlantic. *Prog. Oceanogr.*, **137**, 237–249, https://doi.org/10.1016/j.pocean.2015.06.009.

Peixoto, J. P., and A. H. Oort, 1992: *Physics of Climate*. 1st ed. American Institute of Physics, 520 pp.

Salmon, R., 1986: A simplified linear ocean circulation theory. *J. Mar. Res.*, **44**, 695–711, https://doi.org/10.1357/002224086788401602.

Saravanan, R., and J. C. McWilliams, 1998: Advective ocean–atmosphere interaction: An analytical stochastic model with implications for decadal variability. *J. Climate*, **11**, 165–188, https://doi.org/10.1175/1520-0442(1998)011<0165:AOAIAA>2.0.CO;2.

Sévellec, F., and A. Fedorov, 2013: The leading, interdecadal eigenmode of the Atlantic meridional overturning circulation in a realistic ocean model. *J. Climate*, **26**, 2160–2183, https://doi.org/10.1175/JCLI-D-11-00023.1.

Sutton, R. T., G. D. McCarthy, J. Robson, B. Sinha, A. T. Archibald, and L. J. Gray, 2018: Atlantic multidecadal variability and the U.K. ACSIS program. *Bull. Amer. Meteor. Soc.*, **99**, 415–425, https://doi.org/10.1175/BAMS-D-16-0266.1.

te Raa, L. A., and H. A. Dijkstra, 2002: Instability of the thermohaline circulation on interdecadal timescales. *J. Phys. Oceanogr.*, **32**, 138–160, https://doi.org/10.1175/1520-0485(2002)032<0138:IOTTOC>2.0.CO;2.

——, J. Gerrits, and H. A. Dijkstra, 2004: Identification of the mechanism of interdecadal variability in the North Atlantic Ocean. *J. Phys. Oceanogr.*, **34**, 2792–2807, https://doi.org/10.1175/JPO2655.1.

Timmermann, A., M. Latif, R. Voss, and A. Grötzner, 1998: Northern Hemispheric interdecadal variability: A coupled air–sea mode. *J. Climate*, **11**, 1906–1931, https://doi.org/10.1175/1520-0442(1998)011<1906:NHIVAC>2.0.CO;2.

Tung, K.-K., and J. Zhou, 2013: Using data to attribute episodes of warming and cooling in instrumental records. *Proc. Natl. Acad. Sci. USA*, **110**, 2058–2063, https://doi.org/10.1073/pnas.1212471110.

Veronis, G., 1975: The role of models in tracer studies. *Numerical Models of the Ocean Circulation*, National Academy of Science, 133–146.

Wang, J., B. Yang, F. C. Ljungqvist, J. Luterbacher, T. J. Osborn, K. R. Briffa, and E. Zorita, 2017: Internal and external forcing of multidecadal Atlantic climate variability over the past 1200 years. *Nat. Geosci.*, **10**, 512–517, https://doi.org/10.1038/ngeo2962.

Weaver, A. J., and E. S. Sarachik, 1990: On the importance of vertical resolution in certain ocean general circulation models. *J. Phys. Oceanogr.*, **20**, 600–609, https://doi.org/10.1175/1520-0485(1990)020<0600:OTIOVR>2.0.CO;2.

——, and S. Valcke, 1998: On the variability of the thermohaline circulation in the GFDL coupled model. *J. Climate*, **11**, 759–767, https://doi.org/10.1175/1520-0442(1998)011<0759:OTVOTT>2.0.CO;2.

Winton, M., 1997: The damping effect of bottom topography on internal decadal-scale oscillations of the thermohaline

circulation. *J. Phys. Oceanogr.*, **27**, 203–208, https://doi.org/10.1175/1520-0485(1997)027<0203:TDEOBT>2.0.CO;2.

Wu, L., and Z. Liu, 2005: North Atlantic decadal variability: Air–sea coupling, oceanic memory, and potential Northern Hemisphere resonance. *J. Climate*, **18**, 331–349, https://doi.org/10.1175/JCLI-3264.1.

Zhang, R., R. Sutton, G. Danabosoglu, Y.-O. Kwon, R. Marsh, S. G. Yeager, D. E. Amrhein, and C. M. Little, 2019: A review of the role of the Atlantic meridional overturning circulation in Atlantic multidecadal variability and associated climate impacts. *Rev. Geophys.*, **57**, 316–375, https://doi.org/10.1029/2019RG000644.